Partitioning And Transmuter Research Initiative in a Collaborative Innovation Action

PATRICIA

DELIVERABLE

D5.4 Towards multi-physics description of fuel behaviour for accidental conditions

Author: A. Pérez, J. Wallenius (KTH), M. Di Gennaro, L. Luzzi, A. Magni, D. Pizzocri (POLIMI), X.-N. Chen, A. Rineiski (KIT)

DOCUMENT CONTROL SHEET

DOCUMENT INFORMATION

Document title	Towards multi-physics description of fuel behaviour for accidental conditions
Author(s), (organisation)	A. Pérez, J. Wallenius (KTH), M. Di Gennaro, L. Luzzi, A. Magni, D. Pizzocri (POLIMI), X.-N. Chen, A. Rineiski (KIT)
Document type	Deliverable
Document ID	D5.4
Work package n°	WP5 (Domain: Transmutation)
Work package title	WP5 (WP22) Improvement of modelling and fuel performance codes
Lead beneficiary	KTH
Dissemination level	Public
Date of issue	18/12/2023
Archive ID reference COO	SCK CEN/81540637

DOCUMENT SUMMARY

In the present document, the development of well-structured multi-physics simulation environments to complement fuel performance analysis is presented. The simulation environments are based on information from the sub-channel / reactor scale, i.e., initial and boundary conditions for the fuel pin simulations in off-normal conditions. The environments are developed based on the codes TRANSURANUS, OpenFOAM, SIMMER-III, and BELLA, focused on satisfying the requirements of the code/module to fuel behaviour, with a strong perspective towards the BPJ simulations of concern for the MYRRHA sub-critical core.

The multi-physics environment achieved by POLIMI uses the high-fidelity computational fluid dynamics code OpenFOAM to provide detailed insights into the physics of the behaviour of the primary coolant (LBE) flow within the MYRRHA IPS sub-assembly to the thermo-mechanical analysis at the integral pin level, performed by the fuel performance code TRANSURANUS. The multi-physics environment achieved by POLIMI is developed to assess specifically the MYRRHA fuel pin during normal operation and BPJ transient conditions, exploring different americium contents within the homogeneous strategy (0 – 5 wt.%).

The SIMMER-III code is used by KIT to model the MYRRHA subcritical core and develop a well-structured multi-physics environment, where the IPS subassemblies are filled with various Am-bearing oxide fuels. Two selected Am-bearing fuel cases were calculated for BPJ transients. In the case of the KTH, the multi-physics simulation environment is based on the improvement of BELLA code, developing a thermo-mechanical module considering the feedback with the thermal module, calculating the temperature profiles and the governing thermal-elastic equations, to calculate the stress, displacement, and gap width in the fuel rod.

The results obtained using the multi-physics simulation environments support the design optimization and safety assessment of the MYRRHA fuel pin during normal irradiation and transient scenarios. As well, it will be used in the activity associated with Task 6.2 of the PATRICIA Project, focused on the in-depth, complete analysis of multiple BPJ scenarios, to identify the worst case and hence draw conservative conclusions on the MYRRHA pin safety under irradiation.

DOCUMENT HISTORY

Version	Status	Date
v0	Draft	28/07/2023
v1	Draft	27/11/2023
v2	Draft	05/12/2023
v3	Final	13/12/2023

DOCUMENT APPROVAL

The author, WP Leader and Coordinator acknowledge and accept delivery of the work completed for this deliverable.

Date	Author(s)	Organisation
13/12/2023	Alejandría Pérez, Janne Wallenius	KTH
	Martina Di Gennaro, Lelio Luzzi, Alessio Magni, Davide Pizzocri	POLIMI
	Xue-Nong Chen, Andrei Rineiski	KIT

Date	WP Leader	Organisation
15/12/2023	Lelio Luzzi	POLIMI

Date	Coordinator	Organisation
18/12/2023	Paul Schuurmans	SCK CEN

DISTRIBUTION LIST

Project Officer Renata Bachorczyk-Nagy	EC	Copy on PATRICIA SharePoint
PATRICIA Beneficiaries	PATRICIA Consortium	

Table of contents

1   Introduction

In the present document, the development of well-structured multi-physics simulation environments to complement fuel performance analyses at the integral pin level is described. The environments rely on both neutronics and thermal-hydraulics information from the reactor scale, i.e., initial and boundary conditions for the fuel pin simulation in terms of power, neutron flux, and coolant sub-channel, to be applied in both normal operation and off-normal conditions. The codes involved in the development of the extended simulation environments are TRANSURANUS, OpenFOAM, SIMMER, and BELLA.

A well-structured multi-physics simulation environment refers to a set of modules solving different physics and phenomena within one code or via the coupling of different specific codes. In both cases, the main aim is to consider the interconnections and feedback among the different physics considered. In this work, the thermal-mechanical behaviour of the fuel pin is of main interest, hence the multi-physics simulation environments are focused on satisfying the requirements of the code/module on fuel behaviour, with a strong perspective on Gen-IV reactors and particularly on MYRRHA, the fast reactor system targeted by the PATRICIA Project.

To achieve the objective, multiple simulation tools are applied. One of these is the TRANSURANUS code, the fuel performance analysis code of reference at the European level (owned by the European Commission) [1], [2]. This code requires neutronics and thermal-hydraulics information, i.e., multi-physics feedback used as boundary conditions for the fuel pin performance. In this activity, two multi-physics simulation environments are built to serve TRANSURANUS and hence to include the incorporation of capabilities to model coupled neutronics and thermal-fluid dynamics conditions typical of Gen-IV reactors in OpenFOAM and via the use of SIMMER code.

Another simulation environment developed for this task consists in the BELLA code, which includes some modules dedicated to fuel performance analysis and incorporates Am-bearing fuel behaviour modelling capabilities coupled to point neutron kinetics and lumped-parameter coolant thermal-hydraulics.

The development of capabilities to evaluate reactor dynamics and feedback effects (neutronics and thermal-hydraulics-related) are herein focused on the consequences on safety aspects related to the irradiation in MYRRHA (sub-critical core, latest "Revision 1.8" design) of Am-bearing oxide fuels for transmutation purposes. The main safety figures of merit under consideration include the margin to fuel melting, the potential cladding plasticity enhanced by fuel-cladding mechanical interaction, and the evaluation of the cladding outer temperature relevant for corrosion issues by the lead-bismuth eutectic (LBE) coolant.

The deliverable is structured as follows. Section 2 provides a description of the MYRRHA irradiation scenarios considered in this work. Then, Section 3 focuses on the simulation tools adopted for the realization of the multi-physics environments, while in Section 4 the simulation setup is reported. The simulation results and the evaluation of the pin safety against the considered design limits are presented in Section 5. Conclusions and further developments are drawn in Section 6.

2 Description of the MYRRHA irradiation scenario: normal operation and BPJ transient (design version 1.8)

MYRRHA (Multi-purpose hYbrid Research Reactor for High-tech Applications) is conceived as a flexible fast spectrum pool-type reactor research irradiation facility cooled by lead-bismuth eutectic (LBE) and approaching the licensing process in Belgium. The MYRRHA reactor is designed by SCK CEN with two operating modes: the critical mode and the subcritical mode. Current research on MYRRHA focuses on the subcritical core configuration ($k_{eff} \sim 0.93$) driven by an acceleration driven system (ADS) which ensures the continuous injection of high-energy neutrons. The acceleration system consists of a LINAC, being built at the reactor site, with an average proton bean current up to 4 mA capable of accelerating protons up to 600 MeV enabling spallation reactions on heavy atoms such as the lead and bismuth of the coolant, producing multiple instances of high-energy neutrons [3], [4].

The reactor core is composed of 163 wrapped fuel assemblies (FAs) arranged in a hexagonal lattice with a central position and seven radial rings (Figure 1). The assembly lattice is shrouded by a stainless steel jacket, which helps to keep the various sub-assembly together and reduces the neutron-induces dose on the core barrel [5], and wrapped by a cylindrical core barrel. The design of the subcritical core configuration of the MYRRHA reactor foresees a thermal power output of 70 MW$_{th}$ produced among 78 fuel assemblies, each one consisting of 127 wire-wrapped cylindrical fuel elements with a tight triangular arrangement. These 78 fuel assemblies are surrounded by 42 reflector assemblies with bundles of magnesium oxide MgO rods and 30 dummy assemblies filled with LBE. This core configuration includes also the presence of: the central spallation target assembly which hosts the accelerator proton beam tube and window, 6 in-pile test section (IPS) assemblies, positioned in the second concentric ring of the core (around the central spallation target) and dedicated to material testing and experimental irradiation with fast neutron fluxes of innovative fuel pins fuelled e.g., with Am-MOX fuel, 3 thermal islands for the production of molybdenum-99 and 3 boron carbide B$_4$C control rod bundles.
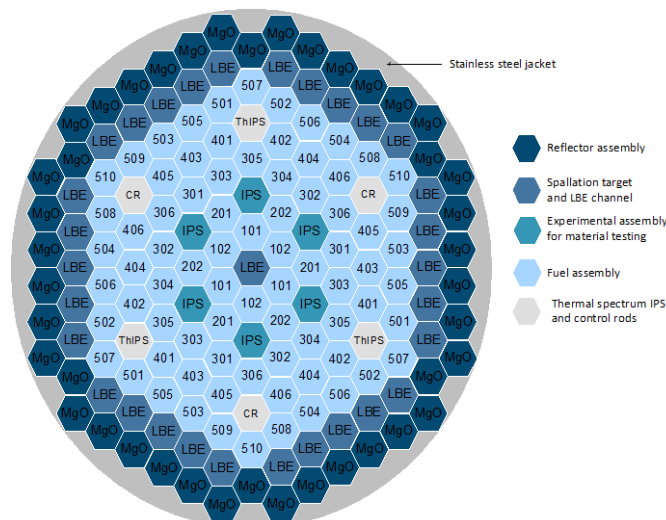
Figure 1: MYRRHA subcritical core layout according to the current design "Revision 1.8".

The 78 FAs are grouped in batches and their subdivision into batches follows the core 1/3rd azimuthal symmetry around the central assembly, making each batch be composed of three FAs. Each batch is identified by a three-digits number, where the first digit indicates the core radial crown where the FA is located, and the second and third digits represent a counter with an increasing order to distinguish batches with different burnup levels (the counter increases with burnup) [6].

At the beginning-of-life (BoL) the core is fully loaded with fresh FAs fueled with U-Pu or U-Pu-Am (PATRICIA option) mixed-oxides. A typical MYRRHA operating schedule consists of irradiation cycles: each fuel assembly spends about 90 Effective Full Power Days (EFPDs) in a specific batch of the core followed by 30 days of shutdown for core reshuffling, loading, and maintenance [5]. Thirteen cycles representative of the fuel handling strategy were identified, as shown in Figure 2. The core reconfiguration after every irradiation cycle requires that the batches composed of six fuel assemblies are shuffled towards outer regions of the MYRRHA core (in-to-out re-shuffling strategy), and fresh fuel is added close to the central spallation target, in order to compensate the reactivity loss. In this way, the final fuel burnup at the end of the driver irradiation for each fuel element is homogenized (expected to be around 70 MWd/kg$_{HM}$ of the spent fuel). The fuel accumulates in a total of 1170 days under irradiation and reaches a lifetime of 3 years. In Figure 3, the radial, local, and axial power factors of the MYRRHA subcritical configuration are reported.
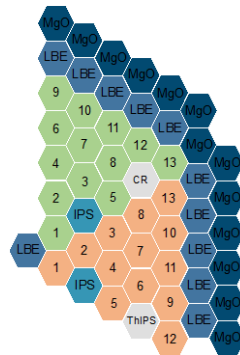

Figure 2: Radial view of 1/3rd of the MYRRHA subcritical core layout at the equilibrium cycle. Numbers indicate the position each FA takes in the core from the moment it is loaded until its discharge [7].
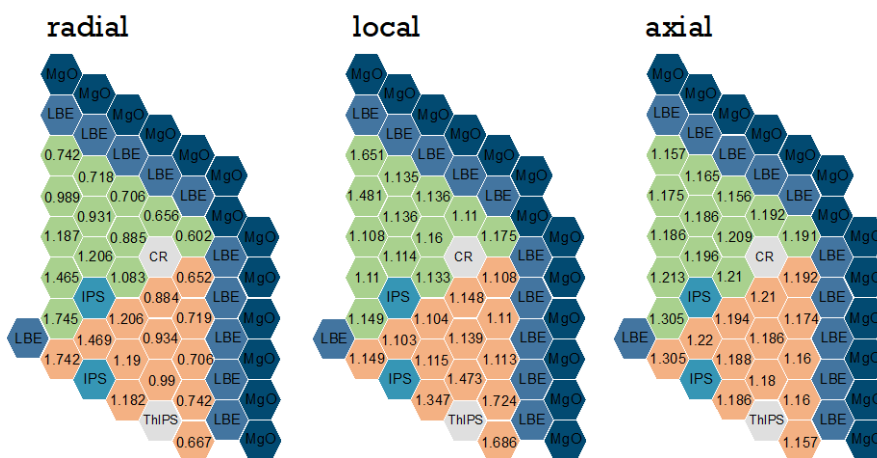

Figure 3: Power factors of the sub-critical core configuration. The radial power factors are calculated as the i-th FA power versus the average FA power, and the local power factors are calculated as the total power of one fuel pin in an assembly versus the assembly-average fuel pin total power. For the axial power factor, only the peak value along the axial power distribution [8].

The fuel considered for MYRRHA within the PATRICIA Project consists of americium-bearing, mixed oxide (Am-MOX) pellets, namely pins fuelled with (U, Pu, Am)O$_{2-x}$, with 95% theoretical density and an oxygen-to-metal ratio (O/M) of 1.97. For what concerns the fuel composition, the current primary option for the MYRRHA core design foresees an amount of plutonium and americium which correspond together to 30 wt.% of the heavy metals in the Am-MOX fuel – see Table 1. In this work, the homogeneous strategy for the recycling and transmutation of americium is analysed: the Am content ranges from 0 to 5 wt.% (limit of a homogeneous recycling strategy), with the reference case study set on 0.49 wt.%. The plutonium content is representative for 90% of plutonium extracted from

the reprocessing of a typical Pressurized Water Reactor (PWR) spent U-oxide fuel (4.5% initial enrichment in ^{235}U, 45 GWd t^{-1} of burn-up, 15 years of cooling and storage) and for 10% of Pu from reprocessed PWR MOX – see Table 1.

Table 1: Elemental composition of the MYRRHA MOX fuel [7], [8].

MOX fuel	Composition (wt.%)
(Pu+Am)/(Pu+Am+U)	30.0
Am/Pu	1.65
U/(Pu+Am+U)	70
O^a	11.672
U^b	61.813
Pu^c	26.078
Am^d	0.437
^{a} O natural isotopic composition: ^{16}O = 99.732 wt.%, ^{17}O = 0.043 wt.%, ^{18}O = 0.225 wt.%. ^{b} U natural isotopic composition: ^{234}U = 0.005 wt.%, ^{235}U = 0.711 wt.%, ^{238}U = 99.284 wt.%. ^{c} Pu natural isotopic composition: ^{238}Pu = 2.332 wt.%, ^{239}Pu = 56.873 wt.%, ^{240}Pu = 26.997 wt.%, ^{241}Pu = 6.105 wt.%, ^{242}Pu = 7.693 wt.%. ^{d} Am natural isotopic composition: ^{241}Am = 100 wt.%.	

The fuel pellets are encased in the austenitic stainless steel DIN 1.4970 cladding, which is a specific alloy, annealed and cold-worked, of the 15-15Ti stainless steel family [9]. Its composition ranges, reported in Table 2, feature trace constituents and a Ti content around 0.5 wt.%, while the 15 wt.% content of the major alloying elements (Ni and Cr) provides the bulk of its thermo-mechanical properties, common to all the steels pertaining to the 15-15Ti family [10]. Ending insulator segments in yttria-stabilized zirconia (YSZ) ceramics are included [11]. In Figure 4, a sketch of the MYRRHA fuel pin is presented.

As primary coolant, the MYRRHA design relies on LBE with 55.5 wt.% Bi and 45.5 wt.% Pb while the secondary coolant is saturated water / steam, with an inlet temperature at the steam generator of 200°C. The LBE core mass flow rate is 9640.93 kg s^{-1} which enters from the bottom of the MYRRHA core with a temperature of 220°C and a pressure of 0.6 MPa.

The design of MYRRHA evolved during the past years as summarized in Table 4. The reference for this work is the MYRRHA design "Revision 1.8", which is a modification of the 1.6 design version and is expected to be completed in 2024. One key modification regards the addition of americium in the MOX fuel to transmute americium in a high flux neutron irradiation and optimize its management. The other one is that all operating temperatures are reduced, mainly aiming to mitigate LBE corrosion in the core region. Based on the results of experimental corrosion studies for the cladding material 15-15Ti [12], it was decided to limit the peak coolant temperature during normal operation to 400°C.

Table 2: Chemical composition of the DIN 1.4970 alloy [5].

			Composition			
Element	B	C	Ca	Co	Cr	Cu
wt.%	0.0030-0.0080	0.080-0.120	≤0.010	≤0.030	14.5-15.5	≤0.050
Element	Mn	Mo	N	Nb	Ni	P
wt.%	≤2.0	1.0-1.4	≤0.015	-	14.5-15.5	≤0.015
Element	S	Si	Ti	Ta	V	
wt.%	≤0.015	0.3-0.6	0.3-0.55	≤0.020	≤0.050	

Table 3: MYRRHA fuel pin design parameters [8].

Parameter	Value
Fuel type	Am-MOX
Fuel density (% of theoretical density)	95
O/M	1.969
As-fabricated porosity (%)	5
Initial fuel grain size (μm)	10
Cladding	DIN 1.4970
Fill gas	He
Fill gas pre pressurization (MPa)	0.1
Fill gas temperature (°C)	20
Lower plenum volume (mm^3)	14541
Upper plenum length (mm)[a]	60
Active length (mm)	650
Lower plenum length (mm)	580
Upper and lower insulator segments length (mm)[b]	35
Upper and lower plug (mm)	20
Total length (mm)	1400
Cladding outer diameter (mm)	6.55
Cladding inner diameter (mm)	5.65
Fuel pellet outer diameter (mm)	5.42
Gap thickness (mm)	0.115
Pin pitch (mm)	8.4
Wire spacer diameter (mm)	1.80
Angle between pin and wire (rad)	0.0988
Wire axial pitch (mm)	265

[a] Assumed that 30% of the upper plenum volume is occupied by the spring.
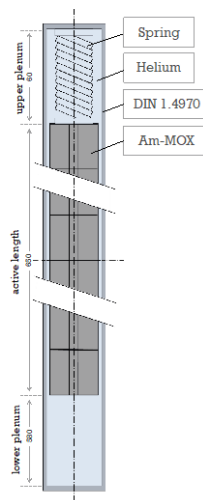[b] Above / below the active length: material made with YSZ.

Figure 4: Sketch of the MYRRHA fuel pin.

Table 4: Overview of the MYRRHA design evolution until current revision 1.8 [13].

Parameter	Unit	Rev. 1.6 [14], [15]	Rev 1.8 [7]
Year	-	2020	2022
Core external diameter	mm	1790	1630
Core height	mm	2500	2500
Core active length	mm	640	650
Vessel internal diameter	mm	10400	8500
Vessel total height	mm	16000	12060
Nominal power subcritical configuration	MW_{th}	70	70
Core inlet temperature	°C	245	220
Maximum temperature against corrosion	°C	450 (outer cladding)	400 (coolant)
Hot plenum temperature	°C	325	275
Number of cycles	-	12	13
Fuel type		MOX	MA-MOX
Max coolant velocity in core	m/s	2.0	2.0

2.1 IPS normal operation

The focus of the analyses performed in this work is the irradiation of a MOX fuel pin loaded with americium in the single-cycle IPS irradiation consisting of 90 days of full power operation. The analysis of the IPS irradiation is particularly of interest to understand the behaviour of Am-MOX fuel during a single MYRRHA cycle, to support the qualification of these pins as driver (or blanket) fuel towards advanced configurations of the reactor core devoted to transmutation / burning goals. The neutron flux and the linear power that a fuel pin experiences in the IPS are assumed as the average between the two surrounding, second-ring driver positions, i.e., number 201 and 202. In particular, the values considered in this work correspond to a hypothetical hottest Am-MOX pin identified as the pin placed in the harshest position (in terms of boundary conditions and temperature) within the fuel assembly. This assumption has been made on purpose to consider the worst irradiation conditions and therefore draw conservative conclusions [7].

2.2 Beam power jump transient

The Beam Power Jump (BPJ) transient is a significant scenario in the ADS sub-critical configuration of MYRRHA [14], [15], initiated by an over-current in the external accelerator during normal reactor operation while the accelerator is working in nominal conditions (beam intensity: 4 mA, beam energy: 600 MeV, reactor core power: 70 MW_{th}). This over-current results in a sudden 70% increase in the proton source, triggering a corresponding 70% rise in the MYRRHA ADS core power due to the proportional relationship between proton current and core power (Figure 5). It is assumed, conservatively neglecting the impact of delayed neutrons, that the reactor power reaches its maximum operating value of 170% within 1 ms without affecting the axial peak factors for the pin linear power (and fast neutron flux). After 3 seconds of sustained high neutron flux, the accelerator undergoes an automatic shut-off, with a scram time of 3 seconds conservatively assumed. Importantly, this tolerance of 3 seconds is specifically designed for the duration of MYRRHA accelerator beam trips, while no

system shut-off is applied to shorter beam trips, allowing them without any limitations on the frequency of occurrence.
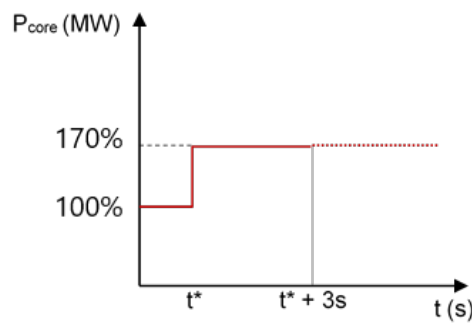

Figure 5: Sketch of the MYRRHA power excursion in a BPJ scenario.

Various BPJ scenarios can be considered, as they have the potential to occur at any moment during normal reactor operation—whether at the outset, midway through, or towards the conclusion of normal irradiation. In this work, the representative BPJ transient is assumed to take place at the conclusion of IPS normal operation.

2.3   Safety limits

A fundamental step towards the licensing phase of the MYRRHA reactor is the design optimization and safety assessment of the fuel pin thermal-mechanical behaviour during both normal operation and transient scenarios. Indeed, compliance with safety requirements must be guaranteed in any scenario of reactor operation. The pin integrity and safety under irradiation are represented by phenomena connected with fuel melting or by cladding mechanical failure.

Regarding the fuel behaviour under irradiation, one design limit is set on the peak fuel temperature, whose maximum value must be lower than the conservative value of 2600°C during any reactor operative condition [16] to avoid any issue related to incipient fuel melting. The fuel temperature limit is derived from the melting (solidus) temperature of the MYRRHA fuel (accounting for its composition and target burn-up), according to data and correlations available in [[17]–[21]]. Considering the initial deviation from the stoichiometry of the MYRRHA fuel (x = 2 – O/M = 0.031) and a conservative upper limit on the fuel burn-up of 10% fissions per initial metal atom (FIMA), the limit of 2600°C mentioned before is confirmed to be conservatively appropriate. For what concerns the cladding structural integrity, it is necessary to avoid its plasticity limiting the plastic strain up to 0.5%. Given the LBE coolant environment, two design limits are imposed on the coolant, based on Russian experiences [22]: the maximum coolant temperature must never exceed 400°C and the maximum coolant bulk velocity is limited to 2 m s^{-1}. The temperature limit imposed on the coolant is necessary to prevent the corrosion mechanism on the cladding outer surface which can potentially degrade the austenitic stainless-steel material depending on the conditions (e.g., type of cladding – coolant materials and coolant flow, oxygen content in the LBE) [23], while the velocity limit is set in order to avoid the erosion of core materials.

3   Multi-physics environments

3.1   SIMMER-III code

SIMMER-III is a 2-dimensional, multi-velocity-field, multiphase, multicomponent, Eulerian, fluid-dynamics computer code, which can be employed with and without a spatial neutron kinetics model [24].

The multi-velocity-field, multi-material-component and multi-phase formulation of SIMMER-III is based on Advanced Fluid Dynamics Model (AFDM), which uses a macroscopic approach and can be applied in simulations with coarse meshes. The heat and mass transfer and the momentum exchange between different phases and materials are modelled explicitly. The conservation equations of fluid mass, momentum and internal energy are solved with a time-factorization approach developed for AFDM [25], in which intra-cell interfacial area source terms, heat and mass transfer, and momentum exchange functions are determined separately from inter-cell fluid convection.

The neutronics part includes two sets of subroutines: (1) for cross-section generation and (2) for spatial kinetics calculations. The cross-section-generation subroutines read data from cross-section libraries with Bondarenko f-factors. For this study, an 11-group cross-section library was used. The effective micro- and macroscopic cross-section calculations are done for each SIMMER fluid-dynamics mesh at each time step, a homogeneous mixture of materials being considered. The temperatures and densities of mixture components (fuel, coolant, structure, etc.) are computed by the fluid-dynamics part of SIMMER. The spatial kinetics calculations are based on the improved quasi-static method, meaning that neutron transport calculations for the flux shape are performed less frequently than point-kinetics calculations for the flux amplitude. Neutron transport calculations are based on the Sn method, using "neutronics" meshes, which are usually parts of larger SIMMER "fluid-dynamics" meshes. The point kinetics calculations are performed by using the cross-sections re-calculated at each time step, the adjoint flux computed at the beginning of the transient, and the time-dependent neutron flux shape. The time-dependent power is computed by the neutronics part by using the time-dependent cross-sections, neutron flux shape and amplitude.

The purpose of SIMMER simulation in this task is to provide the In-Pile Section (IPS) boundary conditions of e.g. power distributions and safety parameters to project partners for their further fuel and core behavior studies.

3.2   OpenFOAM-informed TRANSURANUS with more reliable thermal-hydraulic boundary conditions

In this section, we present the multi-physics simulation environment developed at POLIMI to complement the thermal-mechanical analysis of the fuel pin with more reliable thermal-hydraulic boundary conditions evaluated via computational fluid dynamics calculations. The simulation tool employed for the thermal-mechanical evaluation of the fuel pin under MYRRHA irradiation scenarios is the TRANSURANUS fuel performance code (FPC) [1], [2], [26] developed at JRC-Karlsruhe able to simulate both normal, transient and accidental conditions. TRANSURANUS is a 1.5D computer code, meaning that the thermal and mechanical analysis is performed radially in both fuel and cladding and then the solved radial profiles are coupled between different axial slices of the fuel column. In this work, the computational mesh is configured with 32 axial slices of equal length (20,3 mm each), 47 radial nodes in the fuel, denser towards the gap, and 10 radial nodes in the cladding. The axial mesh nodes are placed at the beginning of the axial slices, as reported in Figure 6, and the input quantities like the linear heat rate and fast neutron flux are constant along the slice.
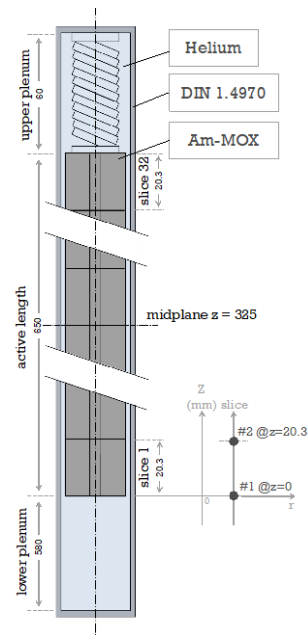
Figure 6. Axial discretization of the fuel pin modelling in the TRANSURANUS code.

For the coolant thermal-hydraulics predictions, TRANSURANUS relies on simplified correlations. The thermo-physical properties of the LBE coolant (e.g., thermal conductivity, specific heat, viscosity) are aligned with the recommendations provided by the latest NEA Handbook [27]. The heat transfer mechanism towards the LBE coolant is suitably described by the correlations reported in Table 5, available in TRANSURANUS. These correlations have been developed from experiments reproducing steady-state conditions, therefore limiting their validity and applicability. In order to improve the prediction of the pin response in different irradiation scenarios, more reliable thermal-hydraulics boundary conditions, evaluated through the finite volume open-source fluid dynamic code OpenFOAM 6.0 [28], are provided to TRANSURANUS.

Table 5. Selected literature correlations for liquid metal heat transfer and hexagonal lattice, where x is the pitch-to-diameter ratio.

Reference	Correlations	Ranges	Fluid
Ushakov et al. 1977 [29]	$Nu = 7.55x - 20x^{-13} + 0.041x^{-2}Pe^{(0.56+0.19x)}$	$1 \leq Pe \leq 4000$ $1.3 \leq x \leq 2.0$	Pb, LBE
Kazimi & Carelli 1976 [30]	$Nu = 4.0 + 0.33x^{3.8}(Pe/100)^{0.86} + 0.16x^{5.0}$	$10 \leq Pe \leq 5000$ $1.1 \leq x \leq 1.4$	Hg, Na, Na-K
Subbotin et al. 1965 [31]	$Nu = 0.58\left(2\sqrt{3}x^2/\pi - 1\right)^{0.55}Pe^{0.45}$	$80 \leq Pe \leq 4000$ $1.1 \leq x \leq 1.5$	LBE

In particular, the Ushakov et al. 1977 and Subbotin et al. 1965 correlations are taken into account as specific for LBE flow, whereas the Kazimi and Carelli 1976 one is chosen on the basis of the good agreement with the experimental data obtained in a hexagonal 19-rod bundle with wire spacers, shown in [32].

The thermal-hydraulics boundary conditions of interest are: the cladding outer temperature and the coolant axial pressure drops. A better understanding of the cladding outer temperature is relevant for the swelling and creep phenomena that impact the cladding geometry influencing in turn the coolant channel, and so the pin coolability [33], and the fuel-cladding gap dynamics reflecting on the fuel temperature regime and cladding mechanical loads [34], [35]. Moreover, the LBE corrosion effects on

the cladding outer surface are influenced by this temperature value. An accurate evaluation of coolant pressure drops allows a better prediction of the (net) mechanical loading acting on the cladding (subjected to the coolant pressure on the outer surface, while to the gas / contact pressure on the inner surface).

The procedure of informing TRANSURANUS calculations with the high-fidelity thermal-hydraulics tool OpenFOAM relies on an offline-online methodology. This methodology consists of the evaluation of the relevant thermal-hydraulics boundary conditions from the LBE coolant side previously mentioned, via an offline, single OpenFOAM simulation of the coolant sub-channel, used then as input data for the online TRANSURANUS calculations targeting the pin thermal-mechanics. The boundary conditions are imported via the definition of the axial peak factors to account for the coolant temperature, pressure and flow rate axial profiles predicted by OpenFOAM.

3.3 BELLA code

BELLA (Bortot's Elegant Liquid LFR Analysis tool) is a computational tool intended for use in the safety-informed, pre-conceptual design of lead-cooled reactor systems, as well as for education and training purposes [36]. BELLA is a plant simulator oriented to the dynamics and control of lead-cooled fast reactors and provides a non-linear solution for the coupled neutron kinetics and thermal-hydraulics of primary and secondary systems. It is based on the use of point kinetics and balance equations for mass, energy, and momentum, which are in general applied to all the primary system components, namely core, steam generator, and pool volumes, such as hot and cold legs. Current capabilities include simulation of unprotected loss-of-flow (ULOF), transient over-power (UTOP), loss-of-heat-sink (ULOHS), and station blackout (ULOF and ULOHS combined) transients for Lead-cooled fast reactors [37]–[39].

BELLA code is a multi-physics environment, which includes seven routines to simulate the neutronic and thermal-hydraulic behavior of the reactor; the reactor core routine solves a set of mass, momentum, and energy equations to calculate the temperature in the coolant, this module is directed coupled with a neutronic module, where the neutronic point kinetic model, coupled with an equation for the reactivity, is solved.
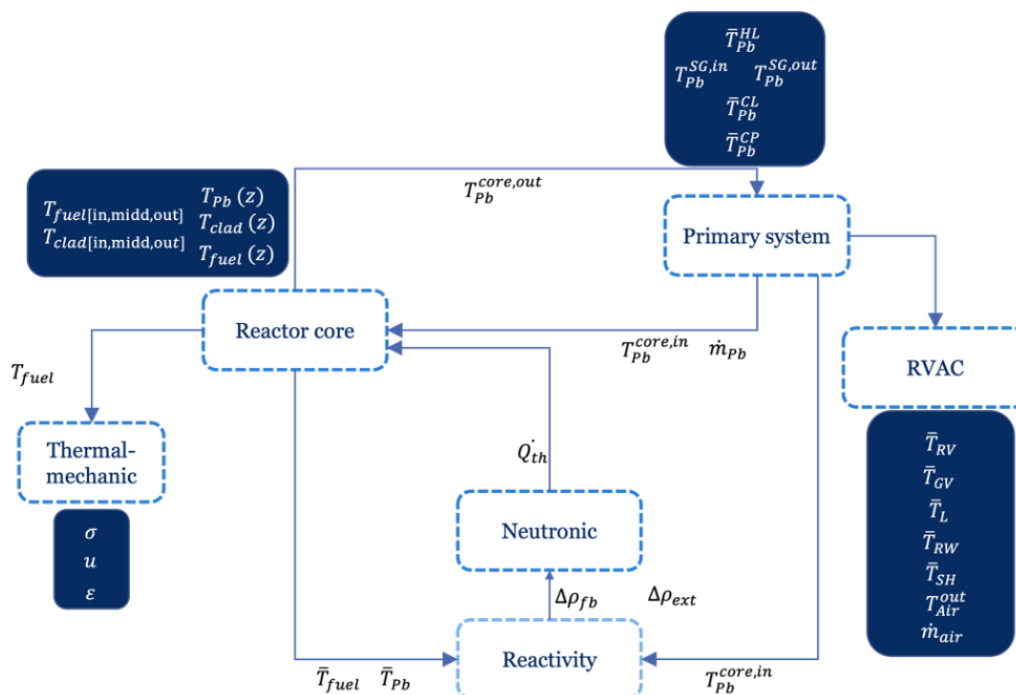

Figure 7. Main modules and feedback in BELLA code.

The primary system module calculates the temperature of the hot leg, steam generator, cold leg, and cold pool, through the solving of a model which includes balances of mass, energy, and momentum. According to the mains of GEN-IV reactors, is important to design a passive safety system, and in the primary system this calculation is included, coupled with the RVAC (Reactor Vessel Auxiliary Cooling System), to calculate the temperatures in the reactor vessel, guard vessel, liner, rock wool, shield and the mass and outlet temperature of the air. In Figure 7, the feedback between the modules on BELLA is shown.

Related to the fuel behavior, in the BELLA code the thermal-mechanic module has been included, in order to develop a well-structured multi-physics simulation environment to simulate the fuel performance. This module includes a set of equations to calculate the stress, displacement, and strain of the fuel. The deformation is calculated as a function of temperature to know the contribution of the thermal expansion. At the same time, those equations are a function of stress, which in turn, is a function of temperature. Furthermore, the displacement is a function of the temperature, impacted directly by the thermal expansion coefficient.

4   Simulation setup

4.1   SIMMER-III simulation setup

4.1.1   Geometric description of the core domain

In this sub-section, the SIMMER-III RZ modeling of MYRRHA subcritical core V1.8 is described. The reactor core and vessel dimensions together with the pump and IHX are established in the SIMMER-III 2-D R-Z cylindrical model. The core includes six types of subassemblies (SAs): 78 fuel assemblies (FAs), 6 In-pile sections (IPSs), 3 control rods (CRs), 3 thermal IPSs, 30 LBE dummy SAs and 42 reflector assemblies. The SIMMER RZ model uses 18 rings in the radial direction to represent these SAs. The fuel assemblies are represented as 5 fuel rings in the active core, which are located at the radial meshes 3, 5, 9, 11, and 15. The IPS subassemblies are assigned to the radial mesh 7 and CRs and thermal IPSs to the radial mesh 13, as shown in Figure 8. In order to take account of the radial heat transfer between SAs in the active region, the coolant flows in narrow inter-wrapper gaps are modelled by the radial meshes 2, 4, 6, 8, 10, 12, 14, and 16. But for LBE dummies and the reflectors, no inter-wrapper gap meshes are assigned. The central radial mesh 1 is for the neutron target unit. The core/IPS fissile height is 65 cm, and it is discretized with 10 axial nodes of 6.5 cm each.
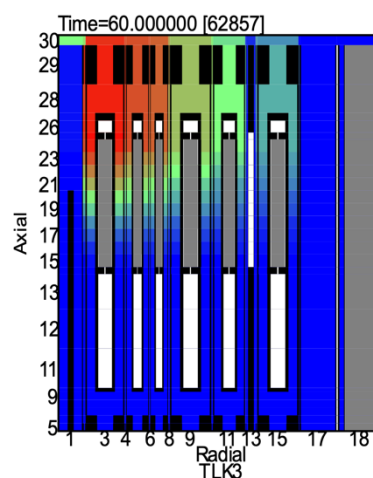

Figure 8. SIMMER III core modeling.

4.1.2   Thermal-hydraulic parameters and models

The main core thermal-hydraulics parameters under steady-state conditions are listed in the following: core power 70 MW$_{th}$ for both steady state and the BPJ transients; pump thrust 2.66 bar; core mass flow rate 71.4 kg/s per FA; coolant inlet temperature 217 °C. The mass flow rate distribution is so gauged that it is radially uniform.

SIMMER steady-state calculations were performed under the following conditions:

- Blasius correlation for basic friction pressure drop.
- The mass flow rate in each FA ring channel was adjusted by adding orifice coefficients.
- Fuel thermal conductivity: Philipponneau correlation [40] with burn-up of 9.8%, O/M ratio 2 - x = 1.96, and porosity of 5%.
- The axial fuel thermal expansion model is included for the computation of transients.
- Cover gas, Xenon is simulated with a default gas model of SIMMER.
- Cover gas pressure: 1 bar
- Pump thrust: 2.66 bar.
- Fuel-clad gap conductance: simulated with a SIMMER option for variable gap conductance with a gas conductivity of 0.25 W/(m K).

4.1.3   Description of fuel compositions

The fuel composition outside IPS is the fuel composition at EOL (end of life), that is irradiated MOX fuel, fabricated without Am, only with U and Pu. After MOX fuel aging and irradiation, a small fraction of Am is present in this fuel, see Table 6. For IPS, 3 fuel compositions: the EOL composition (same as in non-IPS fuel rings), BOL (begin of life) MOX fuel (30% PuOX, 70% UOX) and BOL MOX fuel mixed with 5% of Am-241 oxide (5% AmOX, 25% PuOX, 70% UOX) were used. The same geometry for IPS subassemblies as non-IPS fuel SAs is assumed. The BOL and EOL fuel compositions are given in Table 6, which come from MAXSIMA Project [41]. The Pu content in the BOL fuel is 30.15 wt% and the burn-up in the EOL fuel is 8.28 wt%.

Table 6. BOL and EOL fuel compositions.

HN @BoL		HN @FA EoL		Variation
HN	g/FA	HN	g/FA	(g)
U234	0.00	U234	3.358	3.358
U235	89.32	U235	53.533	-35.787
U236	0.00	U236	8.293	8.293
U237	0.00	U237	0.016	0.016
U238	12315.73	U238	11486.583	-829.147
Np237	0.00	Np237	3.561	3.561
Np238	0.00	Np238	0.002	0.002
Np239	0.00	Np239	1.069	1.069
Pu238	122.80	Pu238	97.660	-25.140
Pu239	2994.34	Pu239	2398.364	-595.976
Pu240	1421.39	Pu240	1430.250	8.860
Pu241	321.41	Pu241	245.991	-75.419
Pu242	405.03	Pu242	374.657	-30.373
Am241	72.64	Am241	93.700	21.060
Am242m	0.27	Am242m	3.473	3.203
Am243	15.41	Am243	43.505	28.095
Pu243	0.00	Pu243	0.006	0.006
Pu244	0.00	Pu244	0.001	0.001
Am242g	0.00	Am242g	0.015	0.015
Cm242	0.00	Cm242	2.982	2.982
Cm243	0.00	Cm243	0.207	0.207
Cm244	0.00	Cm244	8.758	8.758
Cm245	0.00	Cm245	0.552	0.552
Cm246	0.00	Cm246	0.019	0.019
Cm247	0.00	Cm247	0.000	0.000
Cm248	0.00	Cm248	0.000	0.000
Total	**17758.33**	**Total**	**16256.55**	**-1501.77**
(Fission Products ≥ 1 µg)		**Total FP**	**1471.16**

4.1.4   Power distributions in the steady state and feedback coefficients

The coupled calculations were done with the SIMMER code, as transient calculations until a steady-state was reached. Table 7 shows values for different fuel compositions: for k-eff, power at steady-state, and coolant mass-flowrate. The core power is chosen as 70 MW$_{th}$. The SA mass flow rate design value is 71.4 kg/s. It can be seen that the case of EOL fuel in IPS is almost equivalent to that of the 5% Am BOL fuel, in terms of K-eff values, and the more Am content in the IPS fuel, the less k-eff value.

Table 7. K-eff, power and mass flow rate at the steady state in 3 cases of IPS fuels.

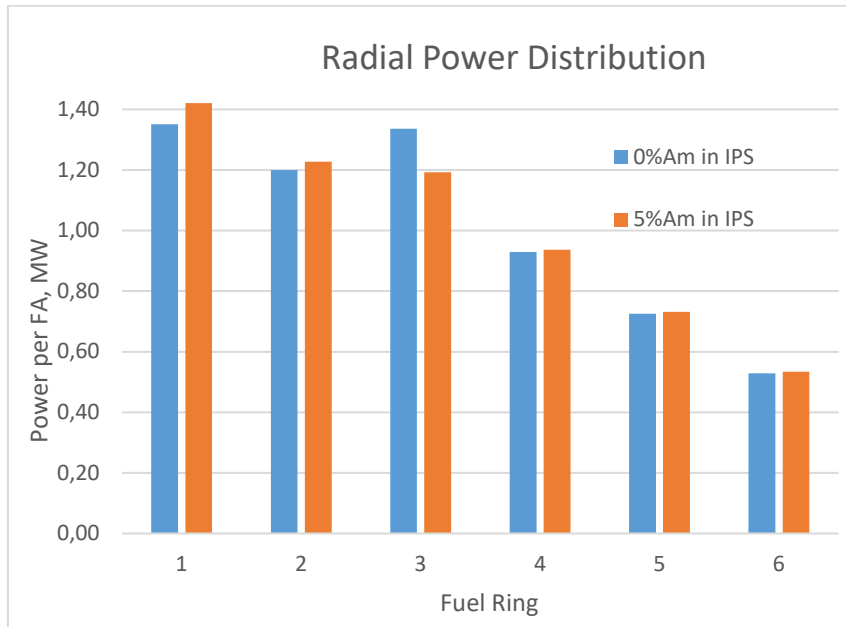| Case of IPS fuel	EOL-fuel	0% Am BOL fuel	5% Am BOL fuel
k-eff	0.934	0.952	0.937
Power (MW)	69.7	69.7	69.7
Mass flow rate per FA (kg/s)	71.6	71.6	71.6

Figure 9. Radial power distributions for 2 cases of Am containing fuels based on BOL MOX fuel, where Fuel Ring 3 is the IPS.
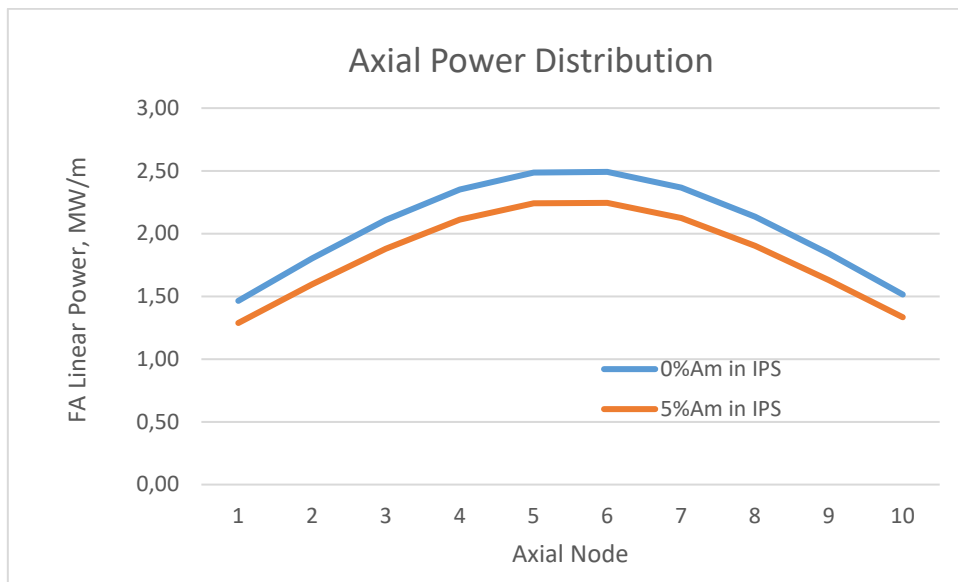

Figure 10. Axial power distributions in IPS for 2 cases of Am containing fuels based on BOL MOX fuel, where the pin linear power can be obtained by dividing the SA value shown here by the number of pins (127).

Figures 9 and 10 show the radial power distributions and axial power distributions in IPS for the 2 cases of Am containing fuels based on BOL MOX fuel. The power in IPS decreases with increased Am contents

because of the lower fission ability of Am. Meanwhile, the power is increasing with increased Am contents in fuel rings 1 and 2, because the radial power shape becomes sharper as the k-eff decreases.

Table 8. Neutronic feedback parameters and coefficients in two cases of IPS fuels.

Parameter	0% Am fuel	5% Am fuel
k-eff	0.95185	0.93708
beta-eff	323.6	321.7
Doppler Constant (pcm)	-263	-264
Coolant Feedback, (pcm/K)	- 0.25235	- 0.24037
Axial Thermal Expansion (pcm/K)	- 0.44565	- 0.41466

Table 8 shows the neutronic feedback parameters and coefficients. The addition of 5% Am in the IPS fuel does not change them significantly and the degradation of the safety parameters is very slight. The Doppler constant value is underestimated in the current cases, where the axial reflector is still. If we replace the axial reflector with Beryllium and fill Beryllium in the 3 CRS and 3 thermal IPS, the Doppler constant is evaluated as -373 pcm for the 0% Am BOL fuel case.

4.2   OpenFOAM simulation setup

4.2.1   Geometric description of the coolant domain

Figure 11 reports a sketch of the hexagonal rod bundle of the IPS sub-assembly characterized by a pitch-to-diameter ratio of 1.28 and an active height equal to 650 mm. The analysis is carried out on the interior sub-channel without considering the presence of the wire-wrapper and preserving the original flow passage area with a mass flow rate of 0.24 kg s^{-1}. Due to the symmetry, only 1/3 of the interior sub-channel is considered as computational domain to simulate, with a hydraulic diameter of 4.86 mm. The mesh generation process was handled with ANSYS Workbench 2023 R1 [42]. After a grid independence study, performed using the coolant temperature as reference output, the finer mesh (mesh number four in Table 9 with fully resolved grid) has been selected for the analysis in this work in order to have a good resolution of the boundary layer. The total length of the meshed channel corresponds to the pin active length plus an additional non-heated zone of 100 mm at the bottom, to obtain a hydraulically developed flow, and an additional buffer zone of 100 mm at the top in order to prevent outlet boundary inconsistencies.
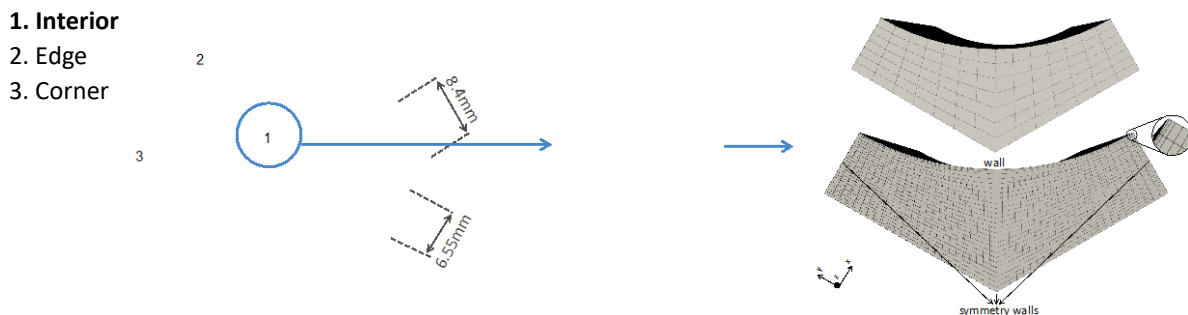

Figure 11. Sketch of the IPS fuel hexagonal sub-assembly and the zoom on the interior sub-channel with the considered computational domain highlighted in blue (left and center). On the right, the coarser (top) and the finer (bottom) meshes of the coolant domain adopted for the grid independence study are shown (Table 9).

Table 9. Main characteristics of the discrete grids employed for the mesh independency study. The mesh 4 is the one selected for the analysis performed in this work.

	Hexaedral elements	Max non-orthogonality	Max skewness	Average y^+	Axial elements	Wall layers
Mesh 1	29'400	26	0.73	40	300	0
Mesh 2	60'000	27	0.75	30	300	0
Mesh 3	240'000	28	0.77	9	300	0
Mesh 4	405'000	29	0.78	~1	300	3

4.2.2 Governing equations and numerical methods

Under the assumption of incompressible fluid, the dynamics of the LBE flow is described by the Navier-Stokes equations coupled with the energy equation under the Boussinesq approximation[1] for density:

$$\frac{\partial \vec{u}}{\partial t} + (\vec{u} \cdot \nabla)\vec{u} - \nabla \cdot (\nu\nabla\vec{u}) = -\frac{1}{\rho}\nabla p - \vec{g}\beta(T - T_{ref}), \tag{1}$$

$$\nabla \cdot \vec{u} = 0, \tag{2}$$

$$\frac{\partial T}{\partial t} + \vec{u} \cdot (\nabla T) = -\nabla \cdot (-\alpha\nabla T). \tag{3}$$

where $\vec{u}$ is the velocity vector, ν is the kinematic viscosity of the fluid, p is the pressure, $\vec{g}$ is the gravity acceleration, β is the thermal expansion coefficient of the fluid, T is the fluid temperature, T_{Ref} is the reference temperature and α is the thermal diffusivity of the fluid.

The RANS approach attempts to directly solve the mean flow properties by employing a Reynolds decomposition of each flow variable $\phi(\vec{x}, t)$ intro its mean component $\overline{\phi}(\vec{x}, t)$ and associated turbulent fluctuations $\phi'(\vec{x}, t)$ which describe the chaotic behaviour of the flow. The scalar ϕ quantity denotes the individual velocity components, u_i with $i = x, y, z$, the pressure and the temperature. By substituting this decomposition into Equations 1, 2 and 3 and averaging over time, the Unstable Reynolds-average Navier-Stokes (URANS) equations are obtained:

$$\frac{\partial \overline{\vec{u}}}{\partial t} + \left(\overline{\vec{u}} \cdot \nabla\right)\overline{\vec{u}} - \nabla \cdot \left(\nu\nabla\overline{\vec{u}}\right) = -\frac{1}{\rho}\overline{\nabla p} - \vec{g}\beta(\overline{T} - T_{ref}) - \nabla \cdot \left(\overline{\vec{u}'\vec{u}'}\right), \tag{4}$$

$$\nabla \cdot \overline{\vec{u}} = 0, \tag{5}$$

$$\frac{\partial \overline{T}}{\partial t} + \vec{u} \cdot \left(\nabla\overline{T}\right) = -\nabla \cdot \left(-\alpha\nabla\overline{T}\right) - \nabla \cdot \left(\overline{\vec{u}'T'}\right) \tag{6}$$

with 9 additional terms represented by the Reynolds stress tensor $-\overline{\vec{u}'\vec{u}'}$ and the turbulent heat transfer $-\overline{\vec{u}'T'}$, corresponding to the mean effects of turbulence transfer of momentum and temperature, respectively.

Through the Boussinesq approximation it is possible to relate the Reynolds stress tensor to the mean rate-of-strain tensor $\bar{\bar{S}} \equiv (\nabla\overline{\vec{u}} + \nabla\overline{\vec{u}}^T)/2$ through an eddy viscosity ν_t as:

$$-\overline{\vec{u}'\vec{u}'} + \frac{2k\delta_{ij}}{3} = 2\nu_t\bar{\bar{S}} \tag{7}$$

---

[1]Assumes that density variations are linear with temperature and play a role only in the buoyancy term.

where k is the turbulence kinetic energy and δ is the Kronecker delta. The same is for the turbulent heat transport term with an eddy diffusivity α_t:

$$-\overline{\mathrm{u}'\mathrm{T}'} = \alpha_t \nabla \overline{\mathrm{T}} \tag{8}$$

Plugging in Equations 7 and 8 into the URANS equations (Equations 4,5, and 6) result in[2]:

$$\frac{\partial \overline{\vec{\mathrm{u}}}}{\partial \mathrm{t}} + \left(\overline{\vec{\mathrm{u}}} \cdot \nabla\right)\overline{\vec{\mathrm{u}}} - \nabla \cdot \left((\nu + \nu_t)\nabla\overline{\vec{\mathrm{u}}}\right) = -\frac{1}{\rho}\nabla\overline{\mathrm{p}^*} - \vec{\mathrm{g}}\beta(\overline{\mathrm{T}} - \mathrm{T}_{\mathrm{ref}}), \tag{9}$$

$$\nabla \cdot \overline{\vec{\mathrm{u}}} = 0, \tag{10}$$

$$\frac{\partial \overline{\mathrm{T}}}{\partial \mathrm{t}} + \vec{\mathrm{u}} \cdot \left(\nabla\overline{\mathrm{T}}\right) = -\nabla \cdot \left(-(\alpha + \alpha_t)\nabla\overline{\mathrm{T}}\right) - \nabla \cdot \left(\overline{\vec{\mathrm{u}}'\mathrm{T}'}\right). \tag{11}$$

The closure problem is hence reduced to modeling the turbulent eddy viscosity ν_t and diffusivity α_t. In the current study, the eddy viscosity model is the $k - \omega$ SST (Shear Stress Transport) [43] which solves 2 additional transport equations for the modeled turbulence kinetic energy k and specific turbulence dissipation rate ω. The turbulence diffusivity α_t is modeled by applying the Reynolds analogy, linking turbulent heat and momentum transfer with a turbulent Prandtl number $Pr_t = \nu_t/\alpha_t$.

In OpenFOAM this system of equations is solved by using the segregate PISO (Pressure Implicit with Splitting of Operators) method. The convection terms are discretized by Gauss upwind scheme and the diffusion terms are treated by Gauss linear corrected scheme.

4.2.3 Properties and conditions of the LBE working fluid

In the present work, temperature-dependent dynamic viscosity, thermal conductivity, and specific heat of LBE are adopted (the corresponding models are collected in Table 10). Based on their slight dependence on temperature according to the models in Table 10, LBE density and thermal expansion coefficient are considered constant with respect to temperature and equal to 10'427 kg m^{-3} and 1.24·10^{-4} K^{-1}. The inlet mass flow rate is set by MYRRHA design to 0.08 kg s^{-1} with an inlet temperature equal to 220°C. The turbulence quantities (kinetic energy and specific dissipation rate) at the inlet are evaluated by using the free-stream values. For the outlet boundary condition, the model uses an outflow condition (zero velocity gradient and fixed value pressure). At the wall (cladding outer surface), the thermal heat flux profile shown in Figure 12 is prescribed based on data provided by SCK CEN and obtained by means of the SERPENT code [44] employed for the neutronic analysis of the sub-critical MYRRHA core, adopting the reference Am-MOX composition (0.49 wt.% Am and 29.5 wt.% Pu). On the other domain walls, symmetric boundary conditions are exerted (Figure 11 - right). These boundary conditions are summarized in Table 11. Figure 13 reports the values attained by the Reynolds, Prandtl and Péclet numbers during both normal operational conditions and transient BPJ scenario in the MYRRHA subcritical core.

---

[2] The $2k\delta_{ij}/3$ term gets absorbed into a modified pressure gradient: $\nabla\overline{\mathrm{p}^*} = \overline{\nabla\mathrm{p}} + 2\mathrm{k}\delta_{ij}/3$.

Table 10. Correlations adopted for the thermo-physical properties of LBE coolant [27], where the temperature T is in Kelvin.

LBE property	Correlation	Validity range
Density (kg m^{-3})	$\rho = 11065 - 1.293 \cdot T$	$400\,K \leq T \leq 1800\,K$
Specific heat (J kg^{-1} K^{-1})	$Cp = 164.8 + 3.94 \times 10^{-2} \cdot T + 1.25 \times 10^{-5} \cdot T^2 - 4.56 \times 10^5 \cdot T^{-2}$	$400\,K \leq T \leq 1100\,K$
Thermal conductivity (W m^{-1} K^{-1})	$k = 3.284 + 1.617 \times 10^{-2} \cdot T - 2.305 \times 10^{-6} \cdot T^2$	$400\,K \leq T \leq 1200\,K$
Dynamic viscosity (Pa s)	$\mu = 4.94 \times 10^{-4} \times \exp(754.1/T)$	$400\,K \leq T \leq 1300\,K$
Thermal expansion coefficient (K^{-1})	$\beta = 1/(8558 - T)$	$400\,K \leq T \leq 1500\,K$

Table 11. Overview of boundary conditions for all the OpenFOAM variables.

Quantity	Symbol	inlet	outlet	wall
Velocity	$\vec{u}$	Flow rate 0.08 kg/s and 10427 of density (flowRateInletVelocity)	Zero-gradient $\partial u/\partial n = 0$ (zeroGradient)	No-slip $\vec{u} = 0$ (noSlip)
Temperature	T	Fixed-value $T = 220°C$ (fixedValue)	Adiabatic $\partial T/\partial n = 0$ (zeroGradient)	Thermal heat flux profile (Figure 12) (codedMixed)
Pressure	p	Zero-gradient $\partial p/\partial n = 0$ (zeroGradient)	Fixed-value $p = 0\,bar$ (fixedValue)	Zero-gradient $\partial p/\partial n = 0$ (zeroGradient)
Turbulence kinetic energy	k	Fixed value $k = 3(u_{inlet}I)^2/2$ (fixedValue)[3]	Outflow $\partial k/\partial n = 0$ Backflow: $k \cdot n = 0$ (inletOutlet)	Fixed value $k = 3(u_{inlet}I)^2/2$ (fixedValue)
Specific turbulence dissipation	ω	Fixed value $\omega = \sqrt{k}/l_T$ (fixedValue)[4]	Outflow $\partial \omega/\partial n = 0$ Backflow: $\omega \cdot n = 0$ (inletOutlet)	Fixed value $\omega = \sqrt{k}/l_T$ (fixedValue)

---

[3] Where I is the turbulence intensity equal to $0.16 \cdot Re^{-\frac{1}{8}}$.

[4] Where l_t is the turbulence length scale, which describe the size of the large energy-containing eddies, equal to $0.07 \cdot D_h$ with D_h the hydraulic diameter.
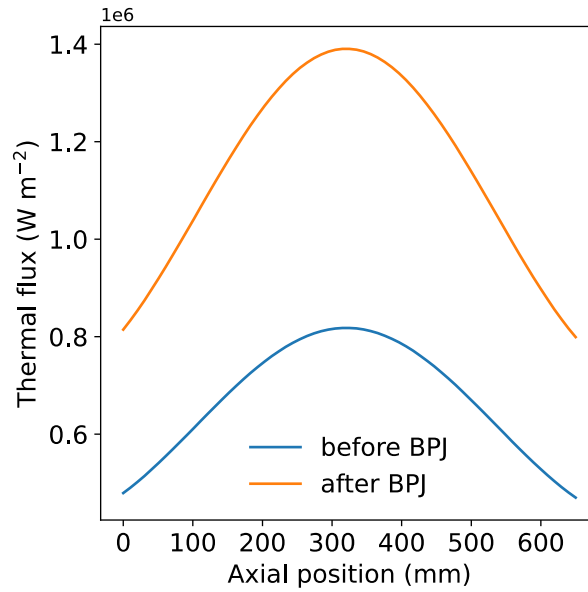
Figure 12. Axial thermal flux profile before and after the BPJ transient imposed as boundary condition in the OpenFOAM simulation.
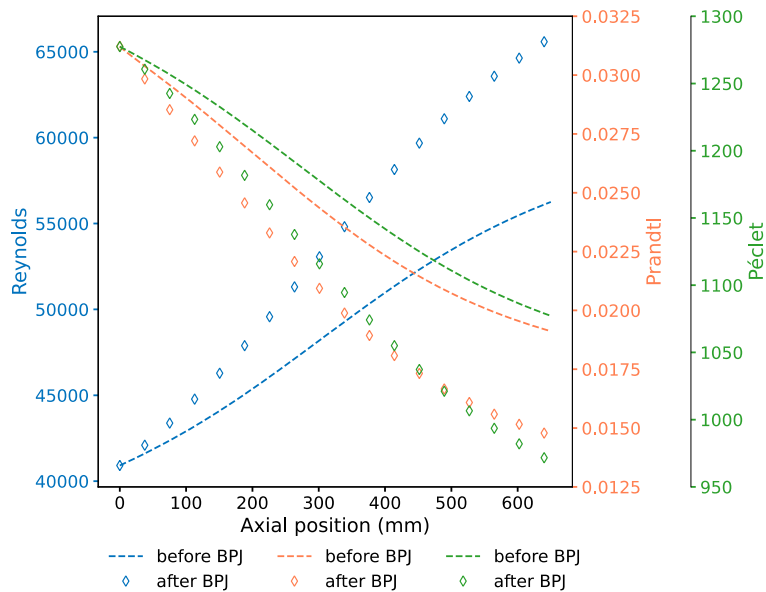

Figure 13. Axial variation of the characteristic non-dimensional number along the length of the sub-channel both, during normal operation (before BPJ) and transient scenario (after BPJ).

4.2.4   Modelling of the turbulent Prandtl number

For the evaluation of the turbulent Prandtl number, several correlations available in literature were explored. All models are summarized in Table 12 and divided in two types according to their independent parameters: the local models depend on local spatial parameters such as y^+ and turbulent Peclet number (defined as $\frac{\nu_t Pr}{\nu}$), instead in the global models no spatial distribution is involved, while they depend on global parameters like Pr, Re and Pe.

Table 12. Turbulent Prandtl number models available in literature.

Reference	Correlation	Range	Remarks
Global models			
Aoki 1963 [45]	$Pr_t^{-1} = 0.014\, Re^{0.45} Pr^{0.2} \left[1 - exp\left(-\dfrac{1}{0.014\, Re^{0.45} Pr^{0.2}}\right)\right]$	$Re \leq 170'000$	
Dwyer 1963 [46]	$Pr_t = 1 - \dfrac{1.82}{Pr\left(\frac{\varepsilon_M}{\nu}\right)_{max}^{1.4}}$		$\varepsilon_M = \dfrac{\nu_t}{\nu}$
Reynolds 1975 [47]	$Pr_t = (1 + 100 Pe^{-0.5}) \left[\dfrac{1}{1 + 120 Re^{-0.5}} - 0.15\right]$	$Re \leq 170'000$	
Jischa and Rieke 1979 [48]	$Pr_t = 0.9 + \dfrac{182.4}{Pr Re^{0.888}}$	$170'000 \leq Re \leq 260'000$	
Myong et al. 1989 [49]	$Pr_t = 0.75 + \dfrac{1.63}{\ln(1 + \frac{Pr}{0.0015})}$		
Cheng and Tak 2006 [50]	$Pr_t = \begin{cases} 4.12 & \\ \dfrac{0.01 Pe}{0.018 Pe^{0.8} - (7.0 - A)^{1.25}} & \end{cases}$	$\begin{cases} Pe \leq 1000 \\ 1000 < Pe \leq 6000 \end{cases}$	$A = \begin{cases} 5.4 - 9 \cdot 10^{-4} Pe & 1000 < Pe \leq 2000 \\ 3.6 & 2000 < Pe \leq 6000 \end{cases}$
Taler 2018 [51]	$Pr_t^{-1} = 0.01592 Re^{0.45} Pr^{0.2} \left[1 - e^{-\left(\frac{1}{0.01592 Re^{0.45} Pr^{0.2}}\right)}\right]$		
Huang et al. 2022 [52]	$Pr_t = 1.5 + 7.745\, e^{(-0.00318 \cdot Pe)}$	$\begin{cases} 56 \leq Pe \leq 2175 \\ 0.01 \leq Pr \leq 0.025 \end{cases}$	
Local models			
Kays and Crawford 1993 [53]	$Pr_t^{-1} = \dfrac{1}{2 Pr_{t\infty}} + C Pe_t \sqrt{\dfrac{1}{Pr_{t\infty}}} - (C Pe_t)^2 \left[1 - exp\left(-\dfrac{1}{C Pe_t}\sqrt{Pr_{t\infty}}\right)\right]$		$Pe_t = \dfrac{\nu_t}{\nu} Pr, C = 0.3$ $Pr_{t\infty} = 0.85$
Kays 1994 [54]	$Pr_t = 0.85 + \dfrac{0.7}{Pe_t}$		$Pe_t = \dfrac{\nu_t}{\nu} Pr$
Weigand et al. 1997 [55]	$Pr_t^{-1} = \dfrac{1}{2 Pr_{t\infty}} + C Pe_t \sqrt{\dfrac{1}{Pr_{t\infty}}} - (C Pe_t)^2 \left[1 - exp\left(-\dfrac{1}{C Pe_t}\sqrt{Pr_{t\infty}}\right)\right]$		$Pe_t = \dfrac{\nu_t}{\nu} Pr, C = 0.3$ $Pr_{t\infty} = 0.85 + \dfrac{100}{Pr Re^{0.888}}$
Liu et al. 2022 [56]	$Pr_t = 0.85 + \dfrac{3.5}{Pe_t}$		
Lei et al. 2022 [57]	$Pr_t = 0.85 + \dfrac{2.5}{Pe_t}$		

Table 13. Overview of methodologies and experimental datasets on heat transfer employed in developing the turbulent Prandtl number models presented in Table 12.

Reference	Data source
Global models	
Aoki 1963 [45]	Semi-empirical approach[5].
Dwyer 1963 [46]	Semi-empirical approach. The coefficients have been chosen to agree with heat transfer measurements made in fully developed pipe flow by Isakoff and Drew 1951 [58] for liquid Hg. The model was tested in pipes, annulus and rod bundles (p/d = 1.75) against the experimental data of Brown et al. 1957 [59] and of Kirillov et al. 1960 [60], the data of Petrovichev 1960 [61] and the data of Friedland et al. 1961 [62], respectively, all for liquid Hg.
Reynolds 1975 [47]	Analytical approach[6].
Jischa and Rieke 1979 [48]	Semi-empirical approach. The coefficients have been chosen to agree with heat transfer measurements made in fully developed pipe flow by Fuchs 1974 [63] for liquid Na, Buhr et al. 1968 [64] and Subbotin et al. 1962 [65] for Hg and Sleicher et al. 1973 [66] for air.
Myong et al. 1989 [49]	RANS simulations (fully developed turbulent pipe flow with constant heat flux for $10^{-2} < Pr < 5 \cdot 10^4$ e $10^4 < Re < 10^5$).
Cheng and Tak 2006 [50]	RANS simulations (fully developed pipe flow with constant heat flux for $140 < Pe < 2800$) and assessment with LBE experimental data of Johnson et al. 1953 [67].
Taler 2018 [51]	Semi-empirical approach. Improved the Aoki 1963 [45] model with the least squares method and based on experimental data of Sheriff et al. 1981 [68] obtained for liquid sodium.
Huang et al. 2022 [52]	LES/DNS simulations (fully developed pipe flow with constant uniform heat flux for $0.01 \leq Pr \leq 0.025$ and $56 \leq Pe \leq 2175$) and assessment in annulars, pipes and bundles.
Local models	
Kays and Crawford 1993 [53]	Semi-empirical approach. The coefficients have been chosen to agree with heat transfer measurements made in fully developed tube flow by Blackwell et al. 1972 [69] for air.
Kays 1994 [54]	The proposed models fit the DNS simulations ([70] and [71]) and then assessed against experimental data of Buhr et al. 1968 [64] for Hg, of Sleicher et al. 1973 [66] for NaK and of Skupinski et al. 1965 [72] for NaK.
Weigand et al. 1997 [55]	Suggests a correction of the Kays and Crawford model grounding on RANS simulations in fully developed turbulent pipe flow with constant heat flux assessed against the experimental data of Skupinski et al. 1965 [72] for liquid NaK and the data of Fuchs 1974 [63] for liquid Na. Assessment against the experimental data of Sleicher et al. 1973 [66] for liquid NaK and of Gilliland et al. 1951 [73] for Hg.
Liu et al. 2022[56]	Improved the Kays model by grounding on LES simulation [74] and experimental data. The model was used to calculate the heat transfer of liquid LBE in fully developed pipe flow and under constant heat flux, and assessed against the Kirrilov correlation [75].
Lei et al. 2022 [57]	Improved the Kays model grounding on DNS simulations ([76], [77]) / LES ([78]) and experimental data of Buhr [64] obtained for Hg and NaK. Assessment against Skupinsky et al. 1965 [72] for NaK and Sleicher et al. 1973 [66] for air.

---

[5] Semi-empirical approach means that it starts from the analytical model and derives the coefficients through the experimental data.

[6] Analytical approach means that the coefficients of the analytical model are chosen to be representative of the type of flow considered.

Figure 14 illustrates the range of values predicted by all the models listed in Table 12 under MYRRHA normal operating conditions.
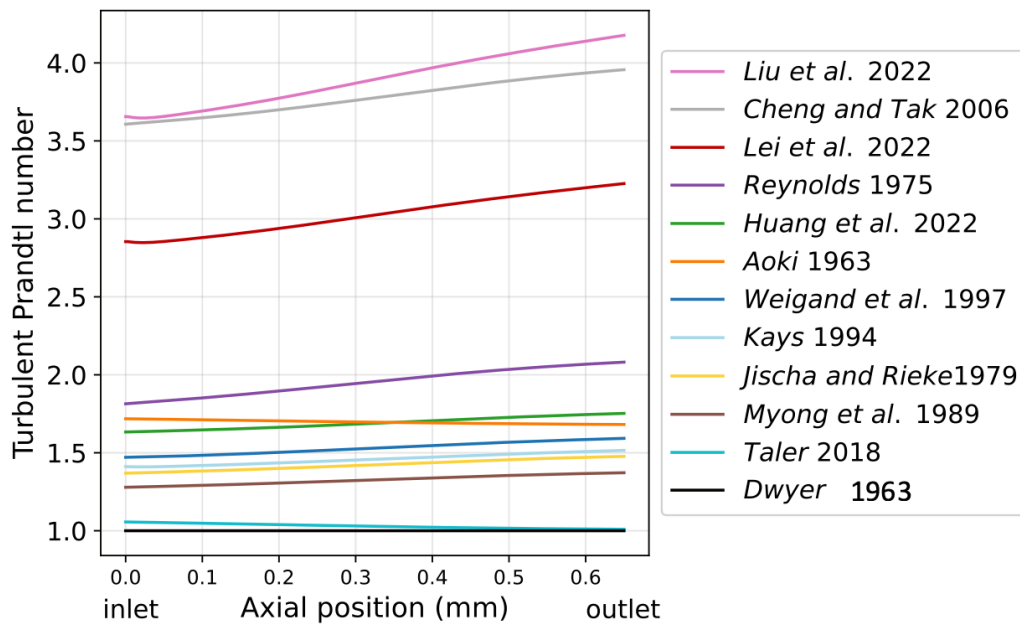

Figure 14. Comparison of the Pr_t along the length of the sub-channel using the different models reported in Table 12 under MYRRHA normal conditions.

Ge et al. 2017 [78] studied the turbulent heat transfer of liquid LBE in the rod bundle sub-channels characterized by pitch-over-diameter ratio of 1.2 and 1.4. They recommend the Pr_t models by Aoki 1963 and Kays 1994, or a constant value equal to 1.5. Based on this recommendation and the literature review performed in Tables 12 and 13, the models by Aoki 1963, Kays 1994 and Huang 2022 were implemented in the OpenFOAM solver in order to perform a sensitivity analysis regarding the impact of different turbulent Prandtl numbers on the heat transfer coefficient. The analysis also involved the constant values of 1.5, as recommended by Ge et al. 2017 [78], and 4, which represents the uppermost value shown in Figure 14.

Figures 15 and 16 illustrate the different heat transfer predicted by the selected models and constant values, presented in terms of the axial Nusselt number and the radial coolant temperature at midplane. The impact of the turbulent Prandtl number varying from 1.5 to 4 is evident in the heat transfer coefficient: Figure 15 highlights a noticeable shift in the Nusselt number, ranging from approximately 17 to about 14, respectively, meanwhile Figure 16 displays a maximum temperature variation of 4°C in the coolant. Both figures underline that, under MYRRHA normal operating conditions, the models by Aoki 1963, Kays 1994 and Huang 2022 predict relatively similar heat transfer coefficients. Furthermore, Figure 15 includes a comparison with the correlations outlined in Table 5, revealing that the results predicted by OpenFOAM using the selected Pr_t models exhibit a good agreement with the Ushakov et al. 1977 [29] correlation.
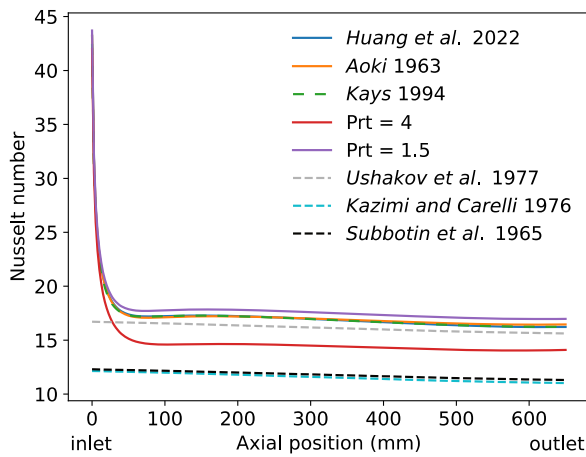
Figure 15. Comparison along the length of the sub-channel of the Nusselt number evaluated using the selected Pr_t models models (by Aoki 1963, Kays 1994 and Huang 2022) and using constant Pr_t equal to 1.5 and 4, under MYRRHA normal operating conditions. The Nusselt numbers predicted by the empirical correlations for LBE reported in Table 5 are additionally reported (dashed lines).
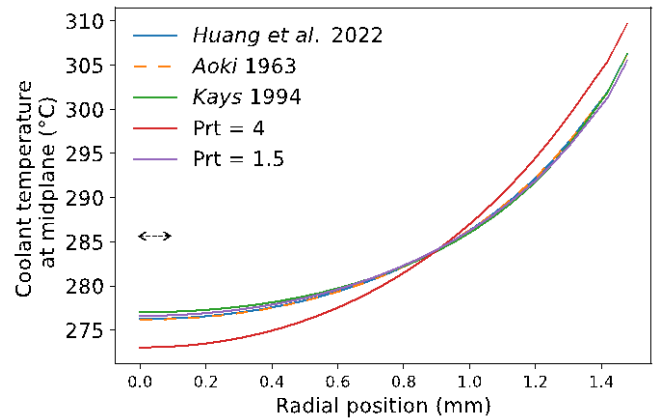

Figure 16. Comparison of the radial coolant temperature at midplane valuated using the selected Pr_t models (by Aoki 1963, Kays 1994 and Huang 2022) and the constant Pr_t equal to 1.5 and 4, under MYRRHA normal operating conditions.

4.3   TRANSURANUS simulation setup

The TRANSURANUS code version adopted in this work, v1m4j22, is equipped with suitable models for the properties of MYRRHA pin materials (fuel and cladding, while the coolant is treated by OpenFOAM – Section 4.2).

For the Am-bearing oxide fuels modelling, the adopted version of TRANSURANUS includes:

- o   The models for the thermal properties (thermal conductivity and melting temperature) proposed and validated in [79] covering the ranges associated to the MYRRHA irradiation in terms of temperature, Am and Pu contents, deviation from stoichiometry, porosity, and burnup, and providing explicit dependencies on the Am content of mixed oxides.
- o   The advanced correlations for mechanical properties (thermal expansion and Young's modulus) proposed in [80].

For the physics-based calculations of inert gas (xenon, krypton, and helium) behaviour within the fuel matrix, TRANSURANUS benefits of the coupling with the grain scale code SCIANTIX, originally developed by Pizzocri et al. 2020 [81]. An advanced version (2.0) of SCIANTIX, object-oriented and with extended modelling capabilities, has been recently developed and assessed [82] and is herein applied. This enables a coherent calculation of fuel swelling and gas release in the fuel-cladding gap resulting from the intra- and inter-granular description of the gas dynamics accounting for lower-length scale data and information embedded in the model parameters (e.g., diffusivities, trapping and re-solution rates, fractional coverage of the grain boundaries). In this way, the FPC benefits from the bridging with the atomistic scale resulting in a consistent multi-scale framework and overcomes the correlation-based modelling typically adopted by engineering software. Moreover, SCIANTIX has also been recently equipped with a surrogate model for the helium production dedicated to the MYRRHA fuel composition and irradiation conditions [7].

For what concerns the models employed for the MYRRHA cladding steel (DIN 1.4970, of the 15-15Ti steels family), TRANSURANUS is equipped with recently developed correlations for the thermal and irradiation-induced creep strain, void swelling, and thermal creep time-to-rupture, applicable to ranges relevant for the current MYRRHA core design [16].

4.4   BELLA simulation setup

4.4.1   Thermo-mechanical simulation

The thermal elastic governing equations considered in the BELLA thermo-mechanical module, for the analysis of fuel performance, are presented in Table 14. The constitutive equations are based on the infinitesimal deformation theory [83].

Table 14. Governing thermal-elastic equations in the thermo-mechanical module in BELLA code.

Phenomenon	Equation
Radial equilibrium equation Radial stress	$$\frac{d\sigma_r}{dr} + \frac{\sigma_r - \sigma_\theta}{r} = 0$$
Geometric equations Radial displacement and strain	$$\varepsilon_r = \frac{du}{dr} \quad \varepsilon_\theta = \frac{u}{r} \quad \varepsilon_z = constant(r)$$
Generalized Hooke´s Law Stress and strain	$$\varepsilon_r = \frac{1}{E}\big(\sigma_r - \nu(\sigma_\theta + \sigma_z)\big) + \alpha T + \varepsilon^s + \varepsilon_r^c$$ $$\varepsilon_\theta = \frac{1}{E}\big(\sigma_\theta - \nu(\sigma_r + \sigma_z)\big) + \alpha T + \varepsilon^s + \varepsilon_\theta^c$$ $$\varepsilon_z = \frac{1}{E}\big(\sigma_z - \nu(\sigma_\theta + \sigma_r)\big) + \alpha T + \varepsilon^s + \varepsilon_z^c$$

Where σ is the stress, ε is the deformation, u is the displacement, E is the Young's elasticity module, ν is the Poisson´s relation, α is the thermal expansion coefficient, and T is the temperature. Subscripts r, θ, z correspond to the cylindrical coordinates. In Figure 17, the axial and radial modeling zone is shown, to solve the set of equations presented previously, radial nodes in fuel pellet and cladding and considered.
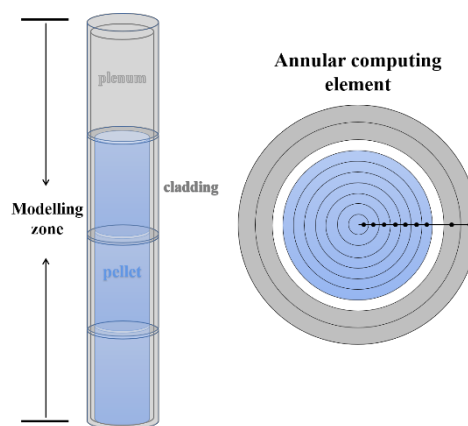

Figure 17. Discretization of the fuel rod (axial and radial) for the thermo-mechanical module.

Based on the set of equations and nodalization, an algorithm to solve it was developed in BELLA code, in Figure 18, the flowchart of the algorithm is shown. The generalized mechanical equations are a function of the temperature, in this case, specifically the temperature of the fuel and cladding. In BELLA code, the temperatures are calculated in the module of the reactor core, solving a set of heat transfer equations, to get radial and axial profiles.

The temperature profiles are the input to calculate the mechanical properties, thermal expansion, and swelling. A material database of fuel and cladding is also included. After the calculation of thermal expansion and swelling, the contact controller verifies if there is a contact between the fuel and cladding and if the fuel is cracked. Once the verification is done, the displacement, stress, strain, and pressure are calculated and sent as an output of the module.
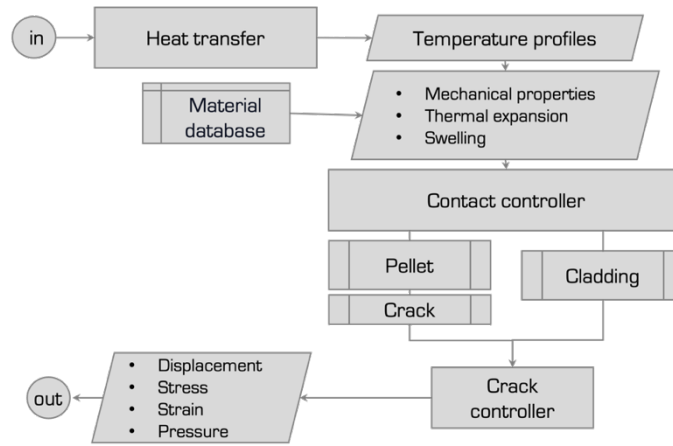

Figure 18. Flowchart of mechanics calculation in thermo-mechanical module.

4.4.2   Fuel, cladding and coolant correlations

In this section, the thermo-physical and mechanical correlations for the properties of fuel (Table 15), cladding (Table 16), and coolant (Table 17) implemented and adopted in BELLA are presented.

Table 15. Thermo-physical and mechanical properties of MOX fuel.

Property	Correlation
Density (kg m^{-3})[84]	$\rho(T) = \rho(273) \cdot (9.9672 \times 10^{-1} + 1.179 \times 10^{-5} \cdot T - 2.42 \times 10^{-9} \cdot T^2 + 1.219 \times 10^{-12} \cdot T^3)^{-3}$ $\rho(273) = 10970 + 490 \cdot y \qquad 0 \le y \le 1$
Thermal expansion (%) [84]	$\alpha(T) = 1.1833 \times 10^{-5} - 5.013 \times 10^{-9} \cdot T + 3.756 \times 10^{-12} \cdot T^2 - 6.12 \times 10^{-17} \cdot T^3$
Specific heat (J kg^{-1} K^{-1}) [84]	$Cp(T) = \dfrac{C_1 \left(\frac{\theta}{T}\right)^2 exp\left(\frac{\theta}{T}\right)^2}{\left[exp\left(\frac{\theta}{T}\right) - 1\right]^2} + 2C_2 T + \dfrac{C_3 E_a exp\left(-\frac{E_a}{T}\right)}{T^2}$ $C_1 = 322.49, C_2 = 1.4679 \times 10^{-2}, C_3 = 8.741 \times 10^7$ $\theta = 587.41, E_a = 18531.7$
Thermal conductivity * (W m^{-1} K^{-1}) [84]–[86]	$\lambda_{TD}(T, x) = 1.158 \left(\dfrac{1}{A(x) + B(x) \cdot T} + 6400 \left(\dfrac{1000}{T}\right)^{5/2} exp\left(-\dfrac{16350}{T}\right) \right)$ $A(x) = 0.035 + 2.85x \,, B(x) = (0.286 - 0.715x) \times 10^{-3}$
Young's module (Pa) [87]	$E = E_s exp(-Bx)(1 + 0.05f)$ $E_s = 2.334 \times 10^{11}[1 - 2.752(1 - D)][1 - 1.0915 \times 10^{-4} \cdot T]$
Poisson ratio (-) [87]	$\nu = E/1.748 \times 10^{11}$

*The thermal conductivity of $(U, Pu)O_{2-x}$ at 100% theoretical density (TD) is described by a sum of two terms representing phonon and electron conduction respectively, where A and B are functions of sub-stoichiometry x.

Measurements of the thermal conductivity of americium oxide [88], [89], in conjunction with theoretical modelling of phonon conductivity [90], [91], indicate that the major effect on thermal

conductivity of americium introduction into MOX fuels derives from the concentration of oxygen vacancies. The oxygen potential for the Am-O system is considerably larger than for Pu-O, which is reflected in the fact that americium oxides typically are fabricated with an O/M ratio of 1.9. We may therefore assume that the above given parametrization of MOX conductivity can be applied to americium bearing fuels if a proper account of the O/M ratio is undertaken.

Table 16. Thermo-physical and mechanical properties of cladding.

Property	Correlation
Density (kg m^{-3}) [10]	$\rho = 7900 \left(\dfrac{1}{1 + \varepsilon_{th}}\right)^3$
Thermal expansion (%) [10]	$\varepsilon_{th} = -3.101 \times 10^{-4} + 1.545 \times 10^{-5} \cdot T + 2.25 \times 10^{-9} \cdot T^2$ $T[°C]$
Specific heat (J kg^{-1} K^{-1}) [92]	$Cp = 431 + 0.77 \cdot T + 8.72 \times 10^{-5} \cdot T^2$ $T[K]$
Thermal conductivity (W m^{-1} °C^{-1}) [10]	$k = 13.95 + 0.01163 \cdot T$ $T[°C]$
Young´s modulus (GPa) [10]	$E = 202.7 - 81.67 \times 10^{-3} \cdot T$ $T[°C]$
Poisson Ratio (-) [10]	$\nu = 0.277 + 6 \times 10^{-5} \cdot T$ $T[°C]$

The thermal-hydraulics module considers the properties of LBE in the function of temperature, the correlations adopted are taken from the NEA Handbook (2015 Edition) on Lead-bismuth Eutectic Alloy and Lead Properties (Table 17).

Table 17. Thermo-physical properties of LBE coolant [27].

Property	Correlation
Density (kg m^{-3})	$\rho = 11065 - 1.293 \cdot T$
Thermal expansion (K^{-1})	$\alpha = 1/(8558 - T)$
Specific heat (J kg^{-1} K^{-1})	$Cp = 164.8 + 3.94 \times 10^{-2} \cdot T + 1.25 \times 10^{-5} \cdot T^2 - 4.56 \times 10^5 \cdot T^{-2}$
Thermal conductivity (W m^{-1} K^{-1})	$k = 3.284 + 1.617 \times 10^{-2} \cdot T - 2.305 \times 10^{-6} \cdot T^2$
Dynamic viscosity (Pa s)	$\mu = 4.94 \times 10^{-4} \cdot \exp(754.1/T)$

The correlations are a function of the temperature and at every time step the properties are calculated and used for thermal and mechanical calculations.

To perform the simulation in the BELLA code, it is necessary to have the neutronic parameters for reactivity feedback, these values were given by KIT (Table 8), obtained by means of the SIMMER code.

5   Simulation results

In this section, the results of Beam Power Jump transient simulations by means of the multi-physics environments, developed within Task 5.4, and previously described (Sections 3 and 4), are presented. The BPJ transient scenario occurring during the IPS single-cycle irradiation was described previously in Section 2.2.

5.1   SIMMER-III results

Two types of BPJ transients (BPJ-1 and BPJ-2) are defined, which are illustrated in Figure 19. In the case of BPJ-1 the beam power after the 70% increase will be constant, while in the case of BPJ-2 after increasing it will decrease to zero at t^*+ 6 sec, which was described previously in Section 2.2. Two IPS fuel cases of 0% Am and 5% Am are selected and calculated. Their results are shown in Figures 20 and 21, where the steady state core power is about 70 MW$_{th}$.

The transient data of IPS linear power, mass flow rate and coolant, clad and fuel temperatures are provided to the project partners for BPJ-2 transients in 0% Am and 5% Am cases. The relative maximal IPS linear power (normalized by its steady state value) is presented in Figures 22 and 23, in comparison with the associated total core power. It is possible to observe that the relative IPS linear power is almost the same as the total core power during the transients.
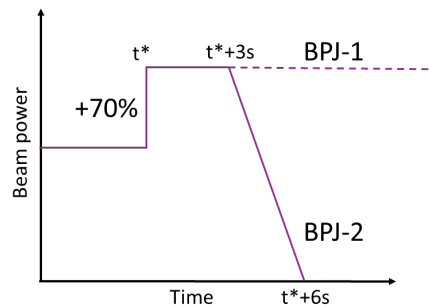

Figure 19. Beam power sketch in BPJ transients for SIMMER simulations, where t^* is the time point of beam power increase start point.
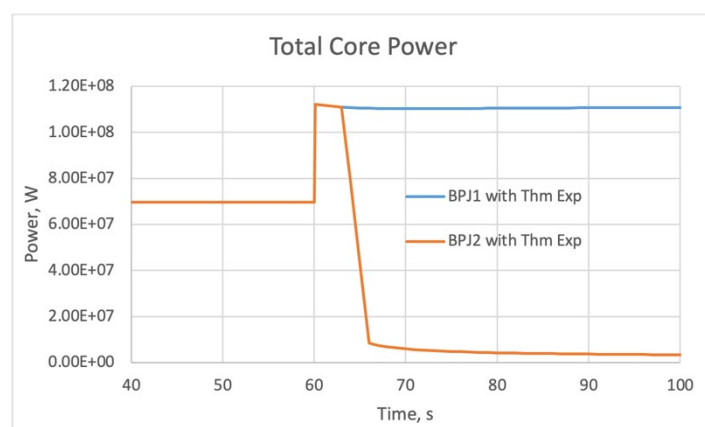

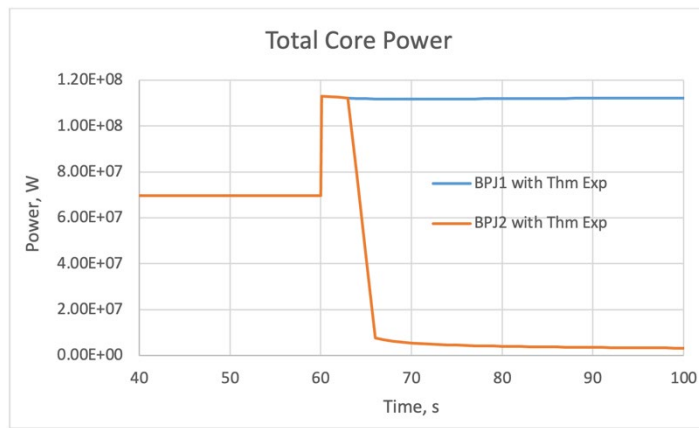Figure 20. Core power during BPJ in the case of 0% Am bearing fuel in IPS.

Figure 21. Core power during BPJ in the case of 5% Am bearing fuel in IPS.
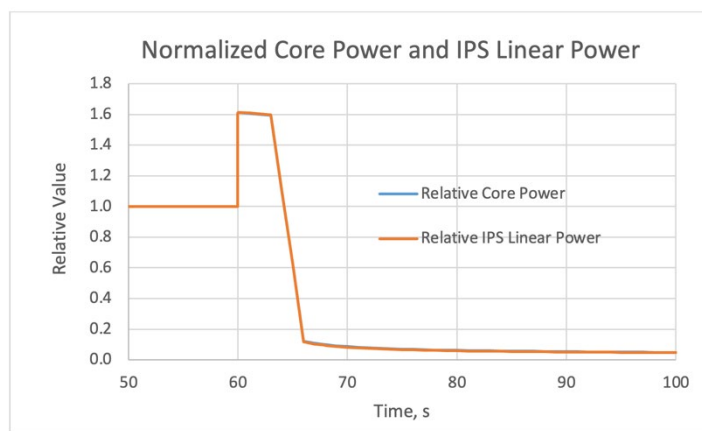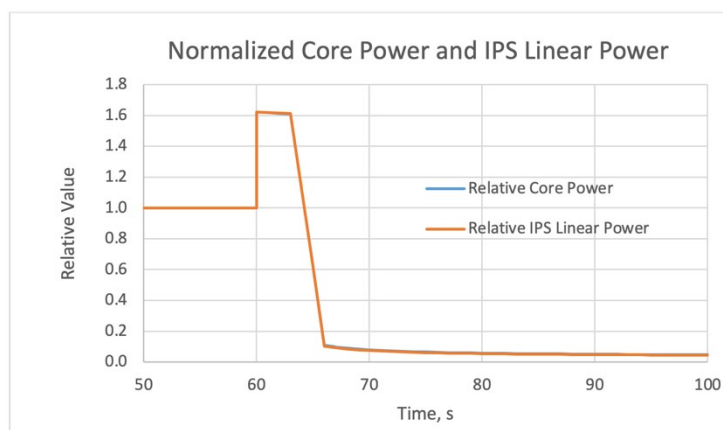

Figure 22. Normalized core power and maximal IPS linear power during BPJ-2 in the case of 0% Am bearing fuel in IPS, where the normalizing core power is 69.63 MW$_{th}$ and the normalizing maximal IPS pin linear power 19.62 kW/m.

Figure 23. Normalized core power and maximal IPS linear power during BPJ-2 in the case of 5% Am bearing fuel in IPS, where the normalizing core power is 69.74 MW$_{th}$ and the normalizing maximal IPS pin linear power 17.68 kW/m.

5.2 OpenFOAM results

This section presents the results obtained via OpenFOAM concerning cladding outer temperature and coolant pressure drops, including both conditions before and after the BPJ transient. The time instant before the BPJ corresponds to the conclusion of a single, normal operation IPS irradiation cycle, i.e., of 90 days of full power in the IPS position within the second ring of the MYRRHA core. Instead, the instant after the BPJ is at the limit of the 3-seconds duration of the +70% power tolerable by the system, just before the accelerator shutdown.

Particular emphasis is on the comparison (shown in Figure 24) of the OpenFOAM high-fidelity results with the TRANSURANUS calculations using the different correlations for the liquid metal heat transfer reported in Table 5. The temperature profile obtained with the Ushakov correlation aligns consistently with the one derived from OpenFOAM, demonstrating coherence in both normal and transient conditions. In contrast, the Kazimi and Subbotin correlations tend to overestimate the cladding outer temperature profile by approximately 7.5°C and 6°C on average, respectively, when compared to the results obtained through OpenFOAM. Furthermore, the discrepancy observed at the inlet of the LBE sub-channel (lowest axial position) is attributed to the development of the thermal boundary layer, an aspect captured by the OpenFOAM simulation but not considered by TRANSURANUS. Instead, the slightly higher active length predicted by TRANSURANUS is due to the axial expansion of the fuel pin not taken into account in the OpenFOAM simulation.
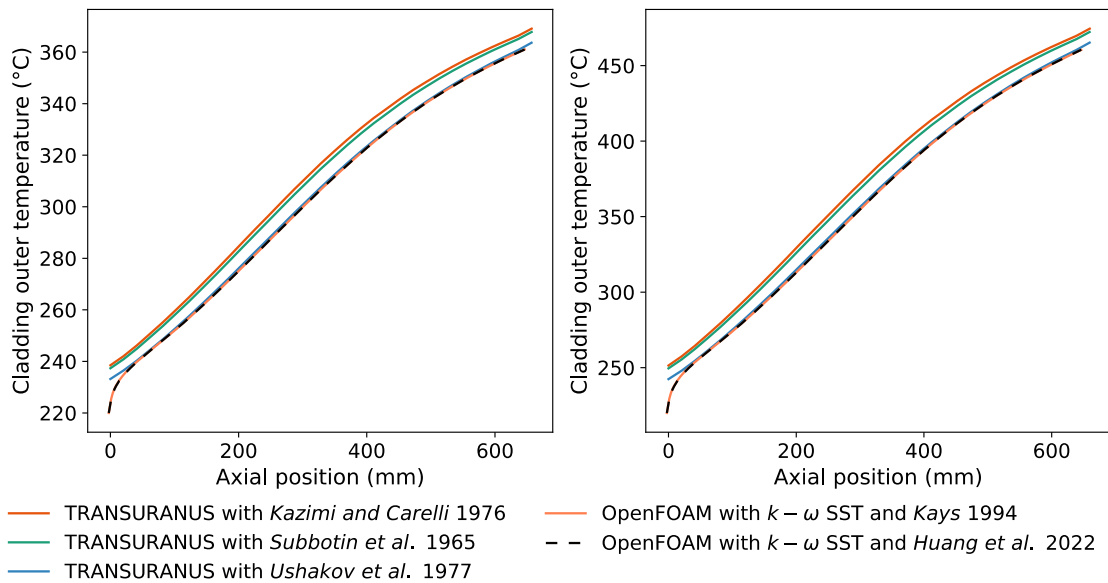

Figure24. Comparison of the cladding outer temperature evaluated via OpenFOAM and TRANSURANUS (by using the correlations in Table 5), before (left) and after (right) the BPJ transient scenario.

Figure 25 reports the total pressure (gravitational and frictional) before and after the BPJ, evaluated via OpenFOAM along the sub-channel length. The observed coolant temperature rise after the BPJ transient leads to a marginal reduction in LBE viscosity and, consequently, contributes to a slight decrease in pressure drops. The total pressure drops between the inlet and the outlet of the sub-channel in normal conditions correspond to 0.114 MPa (aligned with the semi-empirical calculation adopting the Blasius correlation for the friction factor).
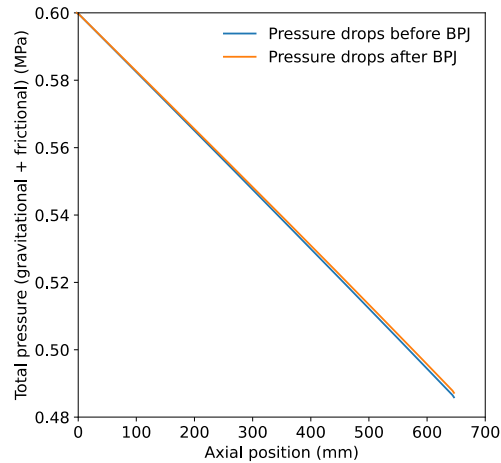
Figure 25. Total LBE pressure drops (gravitational and frictional) evaluated via OpenFOAM (same result from both Huang and Kays correlations for the turbulent Prandtl number).

By employing the CFD simulation, it is also feasible to assess the coolant velocity in the IPS sub-channel (Figure 26), crucial for preventing the erosion of the cladding outer surface by the heavy LBE flowing. The maximum value permitted, 2 m s^{-1}, is reached far away the cladding surface thus avoiding any erosion issues. The average velocity at each axial position corresponds to 1.84 m s^{-1}.
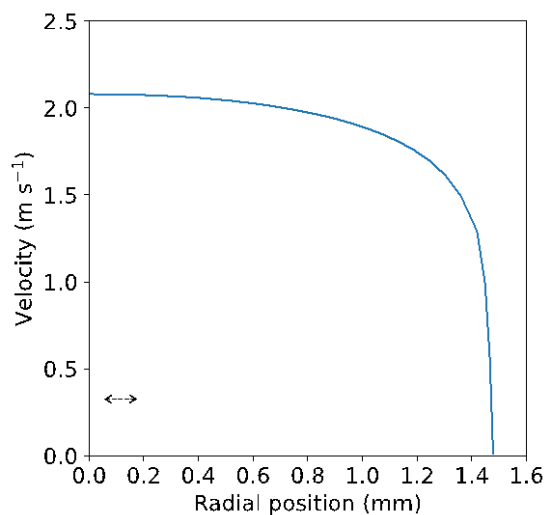

Figure 26. Radial coolant velocity in correspondence of the sub-channel midplane.

5.3 OpenFOAM-informed TRANSURANUS results: fuel pin performance and compliance with MYRRHA design limits

In the current section, we delve into the MYRRHA fuel pin behaviour and assess its safety margins by employing the TRANSURANUS fuel performance code informed by the OpenFOAM results presented in the previous section in terms of coolant pressure and cladding outer temperature (Figure 24 and 25). On the left of Figure 27 the maximum (at the peak power node) linear heat rate (16.87 kW m^{-1}) and fast neutron flux (1.57 · 10^{19} neutrons m^{-2} s^{-1}) history during the MYRRHA-IPS normal irradiation and BPJ transient simulated in TRANSURANUS is shown, while on the right the corresponding axial power profiles before and after the occurrence of the BPJ transient.
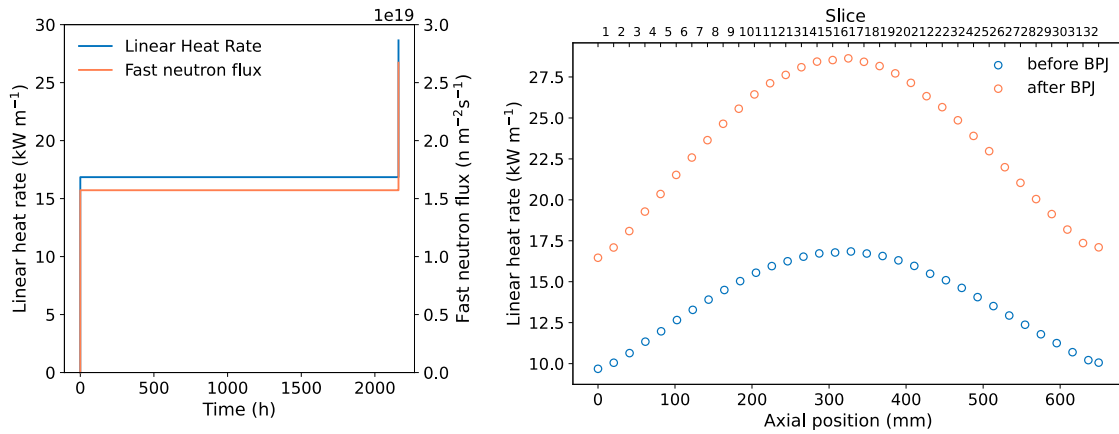
Figure 27. Left: Linear heat rate and fast neutron flux (E > 0.1 MeV) at peak power node of the MYRRHA hottest pin under IPS normal scenario and BPJ transient. Right: Axial power profile before and after the BPJ transient. The values shown correspond to the data provided by SCK CEN obtained through neutronic calculations performed in the SEPRENT code [44] of the sub-critical MYRRHA core with the reference Am-MOX composition (0.49 wt.% Am and 29.5 wt.% Pu).

As depicted in Figure 28, the prescribed safety limit of 400°C for the coolant temperature during MYRRHA normal operation (valid for both the driver and IPS sub-channels), aimed at preventing excessive corrosion of the outer cladding, is respected. Although the design limit is exceeded after the power transient, this is not a concern because the BPJ is a short-lived transient (maximum 3 seconds, after which the reactor is shut-off), whereas corrosion operates on longer time scales.
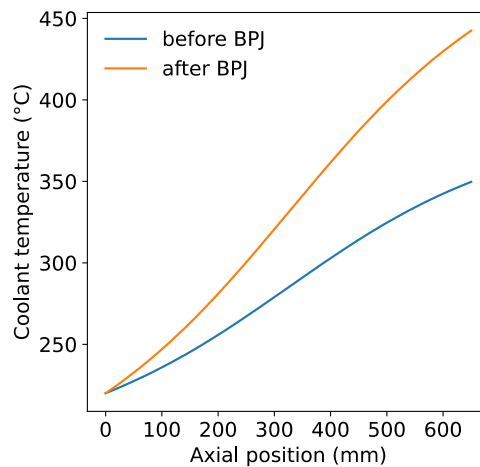

Figure 28. Coolant temperature along the length of the IPS sub-channel, before and after the BPJ transient scenario considered.

Before evaluating the influence of a varying americium content in the Am-MOX MYRRHA fuel, it is necessary to examine how the different cladding temperatures predicted, depicted in Figure 24 impact the performance of the fuel pin. Specifically, the analysis focuses on comparing the TRANSURANUS results using the Kazimi and Carelli 1976 model for heat transfer, which yields the highest cladding outer temperature (Figure 24), and the results obtained by informing TRANSURANUS with the cladding outer temperature and coolant pressure from OpenFOAM, that also accounts for coolant turbulence. The model considered here for the turbulent Prandtl number is the one proposed by Kays 1994 (Table 13).
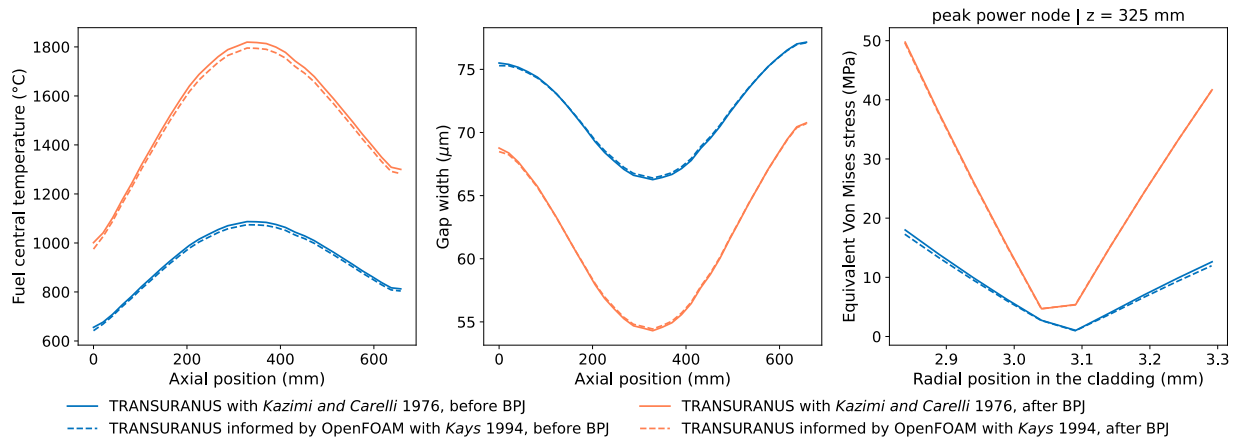
Figure 29. Axial profiles of the fuel central temperature and fuel-cladding gap width (left and centre, respectively), radial profile of the equivalent Von Mises stress at peak power node (right). All the figures of merit are evaluated before (blue) and after (orange) the BPJ transient scenario. The analysis focus on 0.49% of americium concentration.

Under every irradiation condition (nominal / transient), the fuel central temperature never gets close to the design limit imposed on the maximum temperature permitted (2600°C), preventing fuel melting (Figure 18 - left). The fuel central temperature experiences an average change of 10°C before the BPJ when comparing the simulation based on the Kazimi and Carelli 1976 correlation with the TRANSURANUS simulation informed by OpenFOAM. After the BPJ, this temperature shows an average variation of 20°C. As illustrated in the center of Figure 29, no mechanical interaction between fuel and cladding occurs (gap closure) during both normal IPS operation and BPJ transient. The dynamics of the gap take into consideration deformations of both the fuel and the cladding, dominated by the fuel and resulting in a progressive reduction of the gap width during normal operation cycles. In particular, a significant process generally influencing the evolution of the gap is the fuel swelling (together with thermal expansion and creep), that is here simulated via the grain-scale code SCIANTIX [82] coupled to TRANSURANUS. As the gap remains always open during the MYRRHA IPS irradiation, the stress state of the cladding (Figure 18 - right) is influenced solely by the net pressure loading acting on the inner and outer sides of the cladding, determining mechanical stresses, and by the thermal gradient across the cladding, resulting in thermal stresses. From this figure, it is evident that cladding plasticity is consistently avoided under all IPS operational conditions being the equivalent stress well below the yielding stress (approximately 400 MPa at the temperatures associated to BPJ conditions) [16].

In Figure 30, the same figure of merits shown before in Figure 29 is reported, but now the analysis focuses on three americium contents in the homogeneous range (0.49%, 3% and 5%), in order to show the Am impact on the pin performance and safety, predicted by TRANSURANUS informed by OpenFOAM. As shown in Figure 30 - left, the fuel Am content has a relevant impact on fuel central temperature. As reported in [79] the presence of americium degrades the thermal conductivity of the fuel bringing to a lower margin to melting. Even considering a 5% of americium content in the MYRRHA fuel under IPS irradiation, and even under BPJ conditions, the fuel melting is avoided. Moreover, the higher fuel temperature induces a higher thermal expansion of the fuel and this has a strong impact on the residual fuel-cladding gap, which results to be narrower (Figure 30 - center). A higher concentration of americium also results in an increased production of helium. Due to the higher temperature of the fuel containing 5% americium, the release of inert gases (Xe, Kr, He) is greater compared to scenarios with 0.49% and 3% Am contents. Typically, a higher fission gas release leads to an increased pressure in the pin free volume, but this effect is limited in the case of a single IPS cycle.

Consequently, the stress state in the cladding remains the same at different americium contents, as shown in Figure 30 - right.
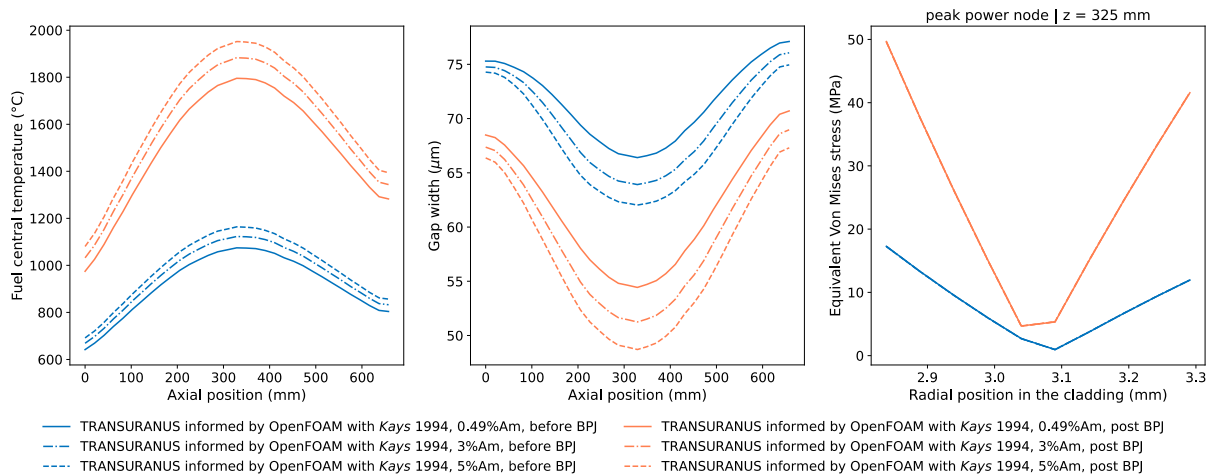

Figure 30. Left and center; Axial profiles of the fuel central temperature and fuel-cladding gap width, Right: Radial profile of the equivalent Von Mises stress at the peak power node. All the figure of merits are evaluated before (blue) and after (orange) the BPJ transient scenario and for three different americium contents: the solid line is for the 0.49% case, the dashed-dot line for the 3% case and the dashed line for the 5% case.

In conclusion, the OpenFOAM-informed TRANSURANUS simulation outcomes reveal a comfortable safety of the designed MYRRHA pins under irradiation, even at the upper limit of americium content (5%) within the range corresponding to the homogeneous strategy, and even during the over-power (BPJ) transient scenario herein considered.

5.4   BELLA results

The simulation of the Beam Power Jump transient performed in the BELLA code is presented below. In Figure 31, the axial temperature profiles are presented, the profiles include the results in steady state (SS), after 3 seconds of starting of BPJ and after 200 seconds of shutdown, to analyze the behavior of the temperature during the event.
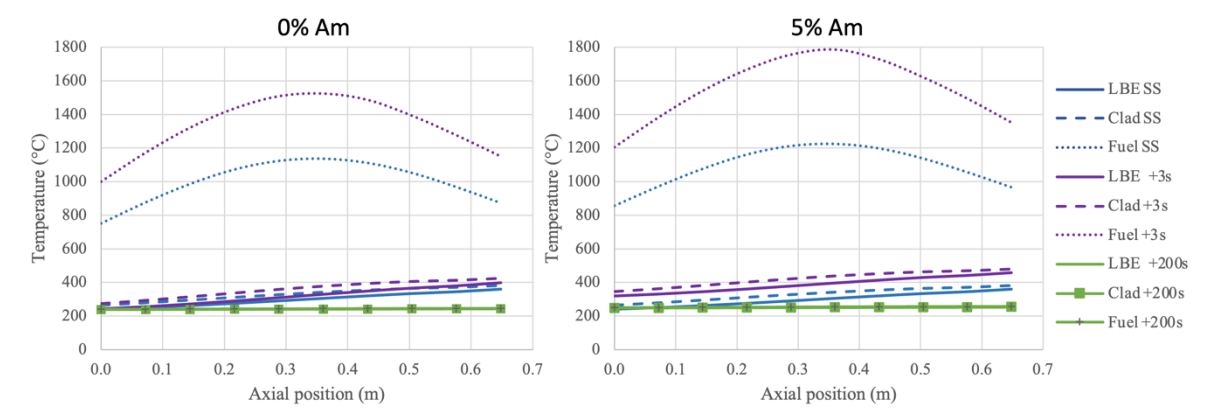

Figure 31. Axial temperature profiles at steady state (SS), 3s after BPJ, and 200s after shutdown, for 0% and 5% Am contents.

The radial temperature profiles are presented in Figure 32, the values correspond to the axial node z = 0.36 m, where the maximum value of temperature is approximated according to the axial profile. In

these profiles is possible to observe that the temperature increases due to the increase of Am. The limit of fuel maximum temperature is the melting point (2600°C), in this simulation, the maximum fuel temperature remains under the limit value.
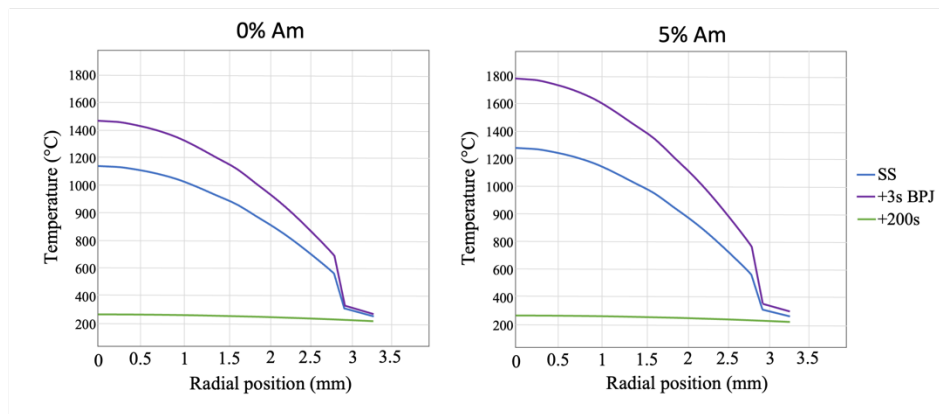
Figure 32. Radial temperature profiles at z=0.35m at steady state (SS), 3s after BPJ, and 200s after shutdown, for 0% and 5% Am contents.

In the BELLA code, the radial temperature profiles are input to the thermal-mechanical module, once this profile is calculated, the stress and displacement are calculated. In Figure 33, the radial and axial stress for the fuel rod is presented. It is possible to observe the increase in stress under the BPJ and, as is expected, due to the increase of Am.

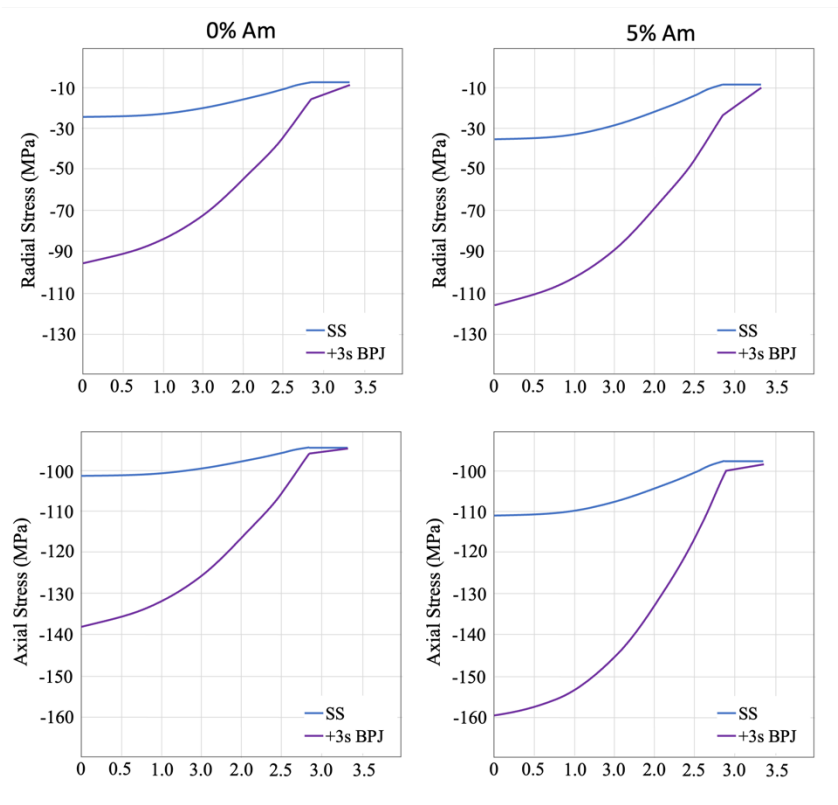Figure 33. Radial and axial stress at steady state (SS) and 3s after BPJ, for 0% and 5% Am contents.
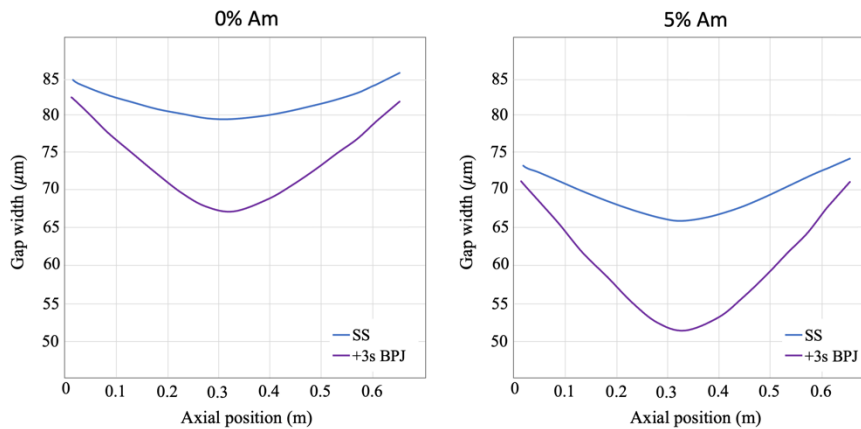
Figure 34. Axial profile of the gap width at steady state (SS) and 3s after BPJ, for 0% and 5% Am contents.

In Figure 34, the axial profile of the gap width is presented, in the case of 0% Am, the displacement in the fuel increases due to the increase in temperature, with a maximum change of 12 μm in the gap width in z = 0.32 m. In the case of 5% Am, the maximum displacement during the BPJ transient is 15 μm in z = 0.32 m, where the gap width is 50 μm.

6   Conclusion and future developments

The goal of Task 5.4 was the development of well-structured multi-physics simulation environments to complement fuel performance analysis with information from the sub-channel / reactor scale, i.e., initial and boundary conditions for the fuel pin simulations in off-normal conditions. The environments were developed based on the codes TRANSURANUS, OpenFOAM, SIMMER, and BELLA, focused on satisfying the requirements of the code/module to fuel behaviour, with a strong perspective towards the BPJ simulations of concern for the MYRRHA sub-critical core.

The aim of the work performed by POLIMI is to provide detailed insights into the physics of the behaviour of the primary coolant (LBE) flow within the MYRRHA IPS sub-assembly, by using the high-fidelity computational fluid dynamics code OpenFOAM. This is done in order to derive more specific and reliable thermal-hydraulics boundary conditions (i.e., cladding outer temperature and coolant pressure drops) to inform the thermo-mechanical analysis at the integral pin level performed by the fuel performance code TRANSURANUS. The multi-physics environment achieved by POLIMI was developed to assess specifically the MYRRHA fuel pin during normal operation and BPJ transient conditions, exploring different americium contents within the homogeneous strategy (0 – 5 wt.%), but the extended simulation tool is suitable to be more generally applied to sub-channels of other reactor core designs.

In the case of KIT, the SIMMER-III code was used and the MYRRHA subcritical core was modelled, where the IPS subassemblies were filled with various Am-bearing oxide fuels. The thermal boundary conditions for the IPS and the core safety parameters were achieved. Two selected Am-bearing fuel cases were calculated for BPJ transients. Results were presented.

The work of KTH was focused on developing a thermo-mechanical module on BELLA code, in this case, the feedback was inside the code, solving the energy balances to calculate the temperature profiles

and the governing thermal-elastic equations, to calculate the stress, displacement, and gap width in the fuel rod.

These multi-physics simulation frameworks support the design optimization and safety assessment of the MYRRHA fuel pin during normal irradiation and transient scenarios. In particular, they are also involved in the activity associated with Task 6.2 of the PATRICIA Project, focused on the in-depth, complete analysis of multiple BPJ scenarios, to identify the worst case and hence draw conservative conclusions on the MYRRHA pin safety under irradiation.

References

[1]   K. Lassmann, "TRANSURANUS: a fuel rod analysis code ready for use," *Journal of Nuclear Materials*, vol. 188, no. C, 1992, doi: 10.1016/0022-3115(92)90487-6.

[2]   A. Magni, A. Del Nevo, L. Luzzi, D. Rozzia, M. Adorni, A. Schubert, P. Van Uffelen, "The TRANSURANUS fuel performance code", in *Nuclear Power Plant Design and Analysis Codes: Development, Validation, and Application*, 2020. doi: 10.1016/B978-0-12-818190-4.00008-5.

[3]   D. De Bruyn, H. A. Abderrahim, P. Baeten, R. Fernandez, J. Engelen, and G. Van Den Eynde, "The MYRRHA ADS project in Belgium enters the Front End Engineering Phase", *International Congress on Advances in Nuclear Power Plants, ICAPP 2014*, 2014. doi: 10.1016/j.phpro.2015.05.012.

[4]   J. Engelen, H. Aït Abderrahim, P. Baeten, D. De Bruyn, and P. Leysen, "MYRRHA: Preliminary front-end engineering design", *International Journal of Hydrogen Energy*, 2015. doi: 10.1016/j.ijhydene.2015.03.096.

[5]   G. Van Den Eynde, E. Malambu, A. Stankovskiy, R. Fernandez, and P. Baeten, "An updated core design for the multi-purpose irradiation facility MYRRHA," *Journal of Nuclear Science and Technology*, vol. 52, no. 7–8, 2015. doi: 10.1080/00223131.2015.1026860.

[6]   L. Fiorito, A. Hernandez-Solis, and P. Romojaro, "Homogenized neutronics model of MYRRHA design revision 1.8." SCK CEN/44767116, 2021.

[7]   L. Luzzi, A. Magni, S. Billiet, M. Di Gennaro, G. Leinders, L. G. Mariano, D. Pizzocri, M. Zanetti and G. Zullo, "Performance analysis and helium behaviour of Am-bearing fuel pins for irradiation in the MYRRHA reactor", Submitted to Nuclear Engineering and Design, 2023.

[8]   European Union's Horizon 2020 Research and Innovation programme, "PATRICIA - Partitioning And Transmuter Research Initiative in a Collaborative Innovation Action," *https://patricia-h2020.eu/*, 2020.

[9]   N. Cautaerts, R. Delville, W. Dietz, and M. Verwerft, "Thermal creep properties of Ti-stabilized DIN 1.4970 (15-15Ti) austenitic stainless steel pressurized cladding tubes", *Journal of Nuclear Materials*, vol. 493, 2017. doi: 10.1016/j.jnucmat.2017.06.013.

[10]   L. Luzzi, A. Cammi, V. Di Marcello, S. Lorenzi, D. Pizzocri, and P. Van Uffelen, "Application of the TRANSURANUS code for the fuel pin design process of the ALFRED reactor," *Nuclear Engineering and Design*, vol. 277, 2014. doi: 10.1016/j.nucengdes.2014.06.032.

[11]   H. Abderrahim, V. Sobolev, and E. Malambu, "Fuel design for the experimental ADS MYRRHA", *Technical Meeting on use of LEU in ADS,* IAEA, Vienna, Austria, no. June 2014, 2005.

[12]   B. Holmstrom, I. Simonovski, F. De Haan, J. Lapetite, D. Baraldi, M. Serrano Garcia, E. Altstadt, J. Aktaa, V. Radu, H. Namburi, C. Cristalli, R. Pohja, R. Delville and A. Courcelle, "Determination of high temperature material properties of 15-15Ti steel by small specimen techniques", EUR 28746 EN, Publications Office of the European Union, Luxembourg, 2017. ISBN 978-92-79-75429-6, doi:10.2760/49859, JRC105589.

[13]   J. Pacio, K. Van Tichelen, G. Kennedy, G. Scheveneels, P. Schuurmans, R. Fernandez, "Experimental Thermal-Hydraulic R&D Achievements And Needs For Myrrha," in *Technical Meeting on State-of-the-art Thermal Hydraulics of Fast Reactors*, 2022. [Online]. Available: https://conferences.iaea.org/event/239/contributions/19794/

[14] A. Magni, M. Bertolus, M. Lainet, V. Marelle, B. Michel, A. Schubert, P. Van Uffelen, L. Luzzi, D. Pizzocri, B. Boer, S. Lemehov, A. Del Nevo, "D7.5-Fuel performance simulations of ESNII prototypes: Results on the MYRRHA case study," 2022. [Online]. Available: www.eera-jpnm.eu/inspyre

[15] A. Magni, M. Di Gennaro, E. Guizzardi, D. Pizzocri, G. Zullo, and L. Luzzi, "Analysis of the performance of driver MOX fuel in the MYRRHA reactor under Beam Power Jump transient irradiation conditions," *Nuclear Engineering and Design*, vol. 414, 112589, 2023. doi: 10.1016/j.nucengdes.2023.112589

[16] A. Magni, T. Barani, F. Bellon, B. Boer, E. Guizzardi, D. Pizzocri, A. Schubert, P. Van Uffelen, L. Luzzi, "Extension and application of the TRANSURANUS code to the normal operating conditions of the MYRRHA reactor," *Nuclear Engineering and Design*, vol. 386, 111581, 2022. doi: 10.1016/j.nucengdes.2021.111581

[17] A. Magni, T. Barani, A. Del Nevo, D. Pizzocri, D. Staicu, P. Van Uffelen, L. Luzzi, "Modelling and assessment of thermal conductivity and melting behaviour of MOX fuel for fast reactor applications," *Journal of Nuclear Materials*, vol. 541, 152410, 2020. doi: 10.1016/j.jnucmat.2020.152410.

[18] W. L. Lyon and W. E. Baily, "The solid-liquid phase diagram for the UO$_2$-PuO$_2$ system," *Journal of Nuclear Materials*, vol. 22, no. 3, 1967, doi: 10.1016/0022-3115(67)90051-7.

[19] E.A. Aitken, and S. K. Evans. "A thermodynamic data program involving plutonia and urania at high temperatures", Nucleonics Laboratory Quart. Rep 3 (1968).

[20] K. Yamamoto, T. Hirosawa, K. Yoshikawa, K. Morozumi, and S. Nomura, "Melting temperature and thermal conductivity of irradiated mixed oxide fuel," *Journal of Nuclear Materials*, vol. 204, no. C, 1993, doi: 10.1016/0022-3115(93)90203-B.

[21] M. Kato, K. Morimoto, H. Sugata, K. Konashi, M. Kashimura, and T. Abe, "Solidus and liquidus temperatures in the UO2-PuO2 system," *Journal of Nuclear Materials*, vol. 373, no. 1–3, 2008, doi: 10.1016/j.jnucmat.2007.06.002.

[22] G. S. Yachmenev, A. E. Rusanov, B. F. Gromov, Yu. S. Belomyttsev, N. S. Skvortsov, and A. P. Demishonkov, "Problems of structural material corrosion in a lead-bismuth coolant," in *Heavy liquid-metal coolants in the nuclear technologies Collection of the conference reports in two volumes, Volume 1*, 1999.

[23] K. Oksana, "Liquid Metal Corrosion Effects in MYRRHA Candidate 316L Austenitic Stainless Steel", Vrije Universiteit Brussel (2018).

[24] S. Kondo, Y. Tobita, K. Morita, N. Shirakawa, "SIMMER-III: An advanced computer program for LMFBR severe accident analysis," *Proceedings of the International Conference on Design and Safety of Advanced Nuclear Power Plant (ANP'92)*, Vol. IV, Tokyo, Japan, 25-29 October 1992, pp.40.5-1 to 40.5-11.

[25] W.R. Bohl, D. Wilhelm, F.R. Parker, J. Berthier, L. Goutagny, H. Ninokata, "AFDM: An Advanced Fluid-Dynamics Model, Vol. I: Scope, Approach, and Summary," LA-11692-MS, Vol. I Los Alamos National Laboratory, (September 1990).

[26] K. Lassmann, "URANUS - A computer programme for the thermal and mechanical analysis of the fuel rods in a nuclear reactor," *Nuclear Engineering and Design*, vol. 45, no. 2, 1978, doi: 10.1016/0029-5493(78)90225-X.

[27] OECD/NEA Handbook, *Handbook on Lead-bismuth Eutectic Alloy and Lead Properties, Materials Compatibility, Thermal- hydraulics and Technologies*, OECD Publishing: Thermal-hydraulics and Technologies, 2015.

[28] "OpenFOAM Foundation", 2018. Accessed: Jun. 19, 2023. [Online]. Available: https://doc.cfd.direct/openfoam/user-guide-v6/

[29] P. A. Ushakov, A. V. Zhukov, and N. M. Matyukhin, "Heat transfer to liquid metals in regular arrays of fuel elements," *Teplofizika vysokikh temperatur,* vol. 15, no 5, p. 1027-1033, 1977.

[30] M. S. Kazimi and M. D. Carelli, "Clinch River Breeder Reactor Plant heat transfer correlation for analysis of CRBRP assemblies," *Westinghouse, CRBRP-ARD-0034*, 1976.

[31] V. I. Subbotin *et al.*, "Heat transfer in elements of reactors with a liquid metal coolant," *Proceedings of the 3rd International Conference on Peaceful Use of Nuclear Energy*, pp. 192–200, 1965.

[32] J. Pacio, M. Daubner, F. Fellmoser, K. Litfin, and T. Wetzel, "Experimental study of heavy-liquid metal (LBE) flow and heat transfer along a hexagonal 19-rod bundle with wire spacers," *Nuclear Engineering and Design*, vol. 301, 2016. doi: 10.1016/j.nucengdes.2016.03.003.

[33] A. L. Pitner, B. C. Gneiting, and F. E. Bard, "Irradiation performance of fast flux test facility drivers using D9 alloy", *Nuclear Technology*, vol. 112, no. 2, 1995, doi: 10.13182/NT95-A35173.

[34] Y. Guerin, "2.21 - Fuel Performance of Fast Spectrum Oxide Fuel," in *Comprehensive Nuclear Materials: Volume 1-5*, 2012. doi: 10.1016/B978-0-08-056033-5.00043-4.

[35] A. E. Waltar, D. R. Todd, and P. V. Tsvetkov, *Fast spectrum reactors*, 2012. doi: 10.1007/978-1-4419-9572-8.

[36] S. Bortot, E. Suvdantsetseg, J. Wallenius, "BELLA: a multi-point dynamics code for safety-informed design of fast reactors", *Annals of Nuclear Energy*, vol. 85, 2015. doi: 10.1016/j.anucene.2015.05.017

[37] J. Wallenius, S. Qvist, I. Mickus, S. Bortot, P. Szakalos, J. Ejenstam, "Design of SEALER, a very small lead-cooled reactor for commercial power production in off-grid applications", *Nuclear Engineering and Design*, vol. 338, 2018. doi: 10.1016/j.nucengdes.2018.07.031

[38] F. Dehlin, J. Wallenius, S. Bortot, "An analytic approach to the design of passively safe lead-cooled reactors", *Annals of Nuclear Energy*, vol. 169, 2022. doi: 10.1016/j.anucene.2022.108971

[39] G. Wang, J. Wallenius, R. Yu, W. Jiang, L. Zhang, X. Sheng, D. Yun, L. Gu, "Transient analyses for China initiative Accelerator Driven System using the extended BELLA code", *Annals of Nuclear Energy*, vol. 190, 2023. doi: 10.1016/j.anucene.2023.109892

[40] Y. Philipponneau, "Thermal conductivity of (U, Pu)O$_{2-x}$ mixed oxide fuel," Journal of Nuclear Materials, vol. 188, p. 194-197, 1992. doi: 10.1016/0022-3115(92)90470-6

[41] M. Sarotto, "Neutronic analysis of maximum cores with the ERANOS deterministic code", *MAXSIMA Semi-Annual Review Meeting, WP2, Task2.1*, April 28-30, 2014, Ghent, Belgium.

[42] Ansys®, "Workbench 2023 R1", 2023. [Online]. Available: https://www.ansys.com

[43] F. R. Menter, "Two-equation eddy-viscosity turbulence models for engineering applications," *AIAA Journal*, vol. 32, no. 8, 1994. doi: 10.2514/3.12149

[44]   J. Leppänen, M. Pusa, T. Viitanen, V. Valtavirta, and T. Kaltiaisenaho, "The Serpent Monte Carlo code: Status, development and applications in 2013," *Ann Nucl Energy*, vol. 82, 2015. doi: 10.1016/j.anucene.2014.08.024

[45]   Aoki S, "A consideration on the heat transfer in liquid metal," *Bulletin of the Tokyo Institute of Technology,* No.54, 1963.

[46]   O. E. Dwyer, "Eddy transport in liquid-metal heat transfer," *AIChE Journal*, vol. 9, no. 2, 1963, doi: 10.1002/aic.690090224

[47]   A. J. Reynolds, "The prediction of turbulent Prandtl and Schmidt numbers", *International Journal of heat and mass transfer*, vol. 18, p. 1055-1069, 1975. doi: 10.1016/0017-9310(75)90223-9

[48]   J. Michael, and H. B. Rieke. "About the prediction of turbulent Prandtl and Schmidt numbers from modeled transport equations", *International Journal of Heat and Mass Transfer*, vol. 22, p. 1547-1555, 1979. doi: 10.1016/0017-9310(79)90134-0

[49]   H. K. Myong, N. Kasagi, And M. Hirata, "Numerical Prediction of Turbulent Pipe Flow Heat Transfe for Various Prandtl Number Fluids with the Improved k-epsilon Turbulence Model," *JSME international journal. Ser. 2, Fluids engineering, heat transfer, power, combustion, thermophysical properties*, vol. 32, no. 4, 1989. doi: 10.1299/jsmeb1988.32.4_613

[50]   X. Cheng and N. Tak, "Investigation on turbulent heat transfer to lead-bismuth eutectic flows in circular tubes for nuclear applications," *Nuclear Engineering and Design*, vol. 236, no. 4, pp. 385–393, 2006. doi: 10.1016/j.nucengdes.2005.09.006

[51]   D. Taler, "Semi-empirical heat transfer correlations for turbulent tube flow of liquid metals", *International Journal of Numerical Methods for Heat and Fluid Flow*, 2018. doi: 10.1108/hff-09-2017-0367

[52]   X. Huang, B. Pang, X. Chai, and Y. Yin, "Proposal of a turbulent Prandtl number model for Reynolds-averaged Navier–Stokes approach on the modeling of turbulent heat transfer of low-Prandtl number liquid metal," *Front Energy Res*, vol. 10, 2022. doi: 10.3389/fenrg.2022.928693

[53]   W. M. Kays and M. E. Crawford, *Convective heat and mass transfer*, New York, McGraw-Hill, Third edition, 1993.

[54]   W. M. Kays, "Turbulent Prandtl Number - Where Are We?", 1994. [Online]. Available: http://heattransfer.asmedigitalcollection.asme.org/

[55]   B. Weigand, J. R. Ferguson, and M. E. Crawford, "An extended Kays and Crawford turbulent Prandtl number model," *International Journal of Heat and Mass Transfer*, vol. 40, no. 17, 1997. doi: 10.1016/S0017-9310(97)00084-7

[56]   H. Liu, Z. Zhang, H. Du, and T. Cong, "Numerical study on the heat transfer characteristics of a liquid lead–bismuth eutectic in a D-type channel," *Front Energy Research*, vol. 10, 2022. doi: 10.3389/fenrg.2022.1041900

[57]   X. Lei, Z. Guo, Y. Wang, and H. Li, "Assessment and improvement on the applicability of turbulent-Prandtl-number models in RANS for liquid metals," *International Journal of Thermal Sciences*, vol. 171, 2022. doi: 10.1016/j.ijthermalsci.2021.107260

[58]   S. Isakoff and T. Drew, "Heat and momentum transfer in turbulent flow of mercury," No. AECU-1199, Columbia University and Brookhaven National Laboratory, 1951.

[59] H. E. Brown, B. H. Amstead, and B. E. Short, "Temperature and Velocity Distribution and Transfer of Heat in a Liquid Metal," *J Fluids Eng*, vol. 79, no. 2, 1957. doi: 10.1115/1.4012982

[60] P. L. Kirillov, V. I. Subbotin, M. Y. Suvorov, and M. F. Troyanov, "Heat-transfer in a tube to sodium-potassium alloy and to mercury," *The Soviet Journal of Atomic Energy*, vol. 6, no. 4, 1960. doi: 10.1007/BF01479731

[61] V. I. Petrovichev, "Heat transfer to mercury in a circular tube and annular channels with sinusoidal heat load distribution," *International Journal of Heat and Mass Transfer*, vol. 1, no. 2–3, 1960. doi: 10.1016/0017-9310(60)90015-6

[62] A. Friedland, O. E. Dwyer, M. W. Maresca, and C. F. Bonilla, "Heat transfer to mercury in parallel flow through bundles of circular rods," *International Heat Transfer Conference*, *Boulder, USA and London,* United Kingdom, 1961.

[63] H. Fuchs, "Heat transfer in flowing sodium: theoretical and experimental investigations on temperature profiles and turbulent temperature fluctuations in a tube," Eidgenoessische Technische Hochschule, Zurich, Switzerland, 1974.

[64] H. O. Buhr, A. D. Carr, and R. E. Balzhiser, "Temperature profiles in liquid metals and the effect of superimposed free convection in turbulent flow," *International Journal of Heat and Mass Transfer*, vol. 11, no. 4, 1968. doi: 10.1016/0017-9310(68)90067-7

[65] V. I. Subbotin, M. K. Ibragimov, M. N. Ivanovskii, M. N. Arnol'dov, and E. V. Nomofilov, "Turbulent heat transfer in a stream of molten metals," *The Soviet Journal of Atomic Energy*, vol. 10, no. 4. 1962. doi: 10.1007/BF01479945

[66] C. A. Sleicher, A. S. Awad, and R. H. Notter, "Temperature and eddy diffusivity profiles in NaK," *Int J Heat Mass Transf*, vol. 16, no. 8, 1973. doi: 10.1016/0017-9310(73)90184-1

[67] H. A. Johnson, J. P. Hartnett, and W. J. Clabaugh, "Heat Transfer to Molten Lead-Bismuth Eutectic in Turbulent Pipe Flow," *J Fluids Eng*, vol. 75, no. 6, 1953. doi: 10.1115/1.4015579

[68] N. Sheriff and D. J. O'kane, "Sodium eddy diffusivity of heat measurements in a circular duct," *International Journal of Heat and Mass Transfer*, vol. 24, no. 2, 1981. doi: 10.1016/0017-9310(81)90028-4

[69] B. F. Blackwell, W. M. Kays, and R. J. Moffat, "the turbulent boundary layer on a porous plate: an experimental study of the heat transfer behavior with adverse pressure gradients," Stanford University, 1972.

[70] J. Kim and P. Moin, "Transport of Passive Scalars in a Turbulent Channel Flow," in *Turbulent Shear Flows 6*, 1989. doi: 10.1007/978-3-642-73948-4_9

[71] N. Kasagi, Y. Tomita, and A. Kuroda, "Direct numerical simulation of passive scalar field in a turbulent channel flow," *J Heat Transfer*, vol. 114, no. 3, 1992. doi: 10.1115/1.2911323

[72] E. Skupinski, J. Tortel, and L. Vautrey, "Determination des coefficients de convection d'un alliage sodium-potassium dans un tube circulaire," *Int J Heat Mass Transf*, vol. 8, no. 6, 1965. doi: 10.1016/0017-9310(65)90077-3

[73] E. R. Gilliland, R. J. Musser, and W. R. Page, "Heat transfer to mercury," *General Discussion on Heat Transfer*, pp. 402–404, 1951.

[74] M. Duponcheel, L. Bricteux, M. Manconi, G. Winckelmans, and Y. Bartosiewicz, "Assessment of RANS and improved near-wall modeling for forced convection at low Prandtl numbers based

on les up to Reτ = 2000," *Int J Heat Mass Transf*, vol. 75, 2014. doi: 10.1016/j.ijheatmasstransfer.2014.03.080

[75]   P. L. Kirillov and P. A. Ushakov, "Heat transfer to liquid metals: Specific features, methods of investigation, and main relationships," *Thermal Engineering*, vol. 48, no. 1, 2001.

[76]   L. Redjem-Saad, M. Ould-Rouiss, and G. Lauriat, "Direct numerical simulation of turbulent heat transfer in pipe flows: Effect of Prandtl number," *Int J Heat Fluid Flow*, vol. 28, no. 5, 2007. doi: 10.1016/j.ijheatfluidflow.2007.02.003

[77]   H. Kawamura, K. Ohsaka, H. Abe, and K. Yamamoto, "DNS of turbulent heat transfer in channel flow with low to medium-high Prandtl number fluid," *Int J Heat Fluid Flow*, vol. 19, no. 5, 1998. doi: 10.1016/S0142-727X(98)10026-7

[78]   Z. Ge, J. Liu, P. Zhao, X. Nie, and M. Ye, "Investigation on the applicability of turbulent-Prandtl-number models in bare rod bundles for heavy liquid metals," *Nuclear Engineering and Design*, vol. 314, 2017. doi: 10.1016/j.nucengdes.2017.01.032

[79]   A. Magni, L. Luzzi, D. Pizzocri, A. Schubert, P. Van Uffelen, and A. Del Nevo, "Modelling of thermal conductivity and melting behaviour of minor actinide-MOX fuels and assessment against experimental and molecular dynamics data," *Journal of Nuclear Materials*, vol. 557, 153312, 2021. doi: 10.1016/j.jnucmat.2021.153312

[80]   S. Lemehov, "New correlations of thermal expansion and Young's modulus based on existing literature and new data", INSPYRE Deliverable D6.3, 2020.

[81]   D. Pizzocri, T. Barani, and L. Luzzi, "SCIANTIX: A new open source multi-scale code for fission gas behaviour modelling designed for nuclear fuel performance codes," *Journal of Nuclear Materials*, vol. 532, 152042, 2020. doi: 10.1016/j.jnucmat.2020.152042

[82]   G. Zullo, L. Luzzi, and D. Pizzocri, "The SCIANTIX code for fission gas behaviour: status, upgrades, separate-effect validation and future developments," *Journal of Nuclear Materials*, vol. 587, 154744, 2023. doi: 10.1016/j.jnucmat.2023.154744

[83]   A. F. Bower, *Applied mechanics of solids*, CRC Press, First Edition, 2009. doi: 10.1201/9781439802489

[84]   J. J. Carbajo, G. L. Yoder, S. G. Popov, and V. K. Ivanov, "A review of the thermophysical properties of MOX and UO_2 fuels," *Journal of Nuclear Materials*, vol. 299, no. 3, 2001. doi: 10.1016/S0022-3115(01)00692-4

[85]   C. Ronchi, M. Sheindlin, M. Musella, and G. J. Hyland, "Thermal conductivity of uranium dioxide up to 2900 K from simultaneous measurement of the heat capacity and thermal diffusivity," *J Appl Phys*, vol. 85, no. 2, 1999. doi: 10.1063/1.369159

[86]   C. Duriez, J. P. Alessandri, T. Gervais, and Y. Philipponneau, "Thermal conductivity of hypostoichiometric low pu content (U, Pu)O_{2-x} mixed oxide," *Journal of Nuclear Materials*, vol. 277, no. 2–3, 2000. doi: 10.1016/S0022-3115(99)00205-6

[87]   D. L. Hagrman, G. A. Reymann, and R. E. Mason, "Matpro — Version 11 A Handbook of Materials Properties for Use in the Analysis of Light Water Reactor Fuel Rod Behavior," *Idaho National Engineering Lab., Idaho Falls (USA)*, vol. 11, no. Revision 2, 1981.

[88] K. Bakker and R. J. M. Konings, "On the thermal conductivity of inert-matrix fuels containing americium oxide," *Journal of Nuclear Materials*, vol. 254, no. 2–3, 1998. doi: 10.1016/S0022-3115(97)00354-1

[89] T. Nishi, M. Takano, A. Itoh, M. Akabori, K. Minato, and M. Kizaki, "Thermal diffusivity of Americium mononitride from 373 to 1473 K," *Journal of Nuclear Materials*, vol. 355, no. 1–3, 2006. doi: 10.1016/j.jnucmat.2006.04.008

[90] S. E. Lemehov, V. Sobolev, and P. Van Uffelen, "Modelling thermal conductivity and self-irradiation effects in mixed oxide fuels", *Journal of Nuclear Materials*, vol. 320, p. 66-76, 2003. doi: 10.1016/S0022-3115(03)00172-7

[91] V. Sobolev, "Thermophysical properties of NpO_2, AmO_2 and CmO_2", *Journal of Nuclear Materials*, vol. 389, p. 45-51, no. 1, 2009. doi: 10.1016/j.jnucmat.2009.01.005

[92] A. Banerjee, S. Raju, R. Divakar, and E. Mohandas, "High temperature heat capacity of alloy D9 using drop calorimetry based enthalpy increment measurements," *Int J Thermophys*, vol. 28, no. 1, 2007. doi: 10.1007/s10765-006-0136-0